Approximating 3D Models of Planetary Evolution in 2D: A Comparison of Different Geometries

Aymeric Fleury[1], Ana-Catalina Plesa[1], Christian Hüttig[1], and Doris Breuer[1]

[1]German Aerospace Center

July 23, 2023

Abstract

Regardless of the steady increase of computing power during the last decades, 3D numerical models continue to be used in specific setups to investigate the thermochemical convection of planetary interiors, while the use of 2D geometries is still favored in most exploratory studies involving a broad range of parameters. The 2D cylindrical and the more recent 2D spherical annulus geometries are predominantly used in this context, but the extent to how well they reproduce the 3D spherical shell in comparison to each other, and in which setup, has not yet been extensively studied. Here we performed a thorough and systematic study in order to assess which 2D geometry reproduces best the 3D one. In a first set of models, we investigated the effects of the geometry on thermal convection in steady-state setups while varying a broad range of parameters. Additional thermal evolution models of three terrestrial bodies, respectively Mercury, the Moon, and Mars, which have different interior structures, were used to compare the 2D and 3D geometries. Our study shows that the spherical annulus geometry improves results compared to cylindrical geometry when reproducing 3D models. Our results can be used to determine for which setup acceptable differences are expected when using a 2D instead of a 3D geometry.

Approximating 3D Models of Planetary Evolution in 2D: A Comparison of Different Geometries

A. Fleury[1], A.-C. Plesa[1], C. Hüttig[1], D. Breuer[1]

[1]Institute of Planetary Research, German Aerospace Center (DLR), Berlin, Germany

Key Points:

- Interior dynamics models using the 2D spherical annulus geometry match the results of a 3D spherical shell better than the 2D cylinder.
- The difference between 2D and 3D geometries decreases when models are heated from below by the core and from within by radioactive elements.
- The spherical annulus shows negligible differences to 3D for the thermal evolution of Mercury and the Moon, and acceptable values for Mars.

Corresponding author: Aymeric Fleury, `aymeric.fleury@dlr.de`

Abstract

Regardless of the steady increase of computing power during the last decades, 3D numerical models continue to be used in specific setups to investigate the thermochemical convection of planetary interiors, while the use of 2D geometries is still favored in most exploratory studies involving a broad range of parameters. The 2D cylindrical and the more recent 2D spherical annulus geometries are predominantly used in this context, but the extent to how well they reproduce the 3D spherical shell in comparison to each other, and in which setup, has not yet been extensively studied. Here we performed a thorough and systematic study in order to assess which 2D geometry reproduces best the 3D one. In a first set of models, we investigated the effects of the geometry on thermal convection in steady-state setups while varying a broad range of parameters. Additional thermal evolution models of three terrestrial bodies, respectively Mercury, the Moon, and Mars, which have different interior structures, were used to compare the 2D and 3D geometries. Our study shows that the spherical annulus geometry improves results compared to cylindrical geometry when reproducing 3D models. Our results can be used to determine for which setup acceptable differences are expected when using a 2D instead of a 3D geometry.

Plain Language Summary

In geodynamic modeling, numerical models are used in order to investigate how the interior of a terrestrial planet evolves from the earliest stage, after the planetary formation, up to present day. The mathematical equations that are used to model the physical processes in the interior of rocky planets are discretized and solved using geometric meshes. The most commonly used geometries are the 3D spherical shell, the 2D cylinder, and the 2D spherical annulus. While being the most accurate and realistic, the 3D geometry is expensive in terms of computing power and time of execution. On the other hand, 2D geometries provide a reduced accuracy but are computationally faster. Here we perform an extensive comparison between 2D and 3D geometries in scenarios of increasing complexity. The 2D spherical annulus geometry shows much closer results to the 3D spherical shell when compared to the 2D cylinder and should be considered in 2D modeling studies.

1 Introduction

Geodynamic modeling is a powerful approach to investigate the dynamics of the mantle and lithosphere of terrestrial planets and to explore the evolution of their interior that is not directly observable. Such models vary in their complexity and often employ different geometries to investigate physical processes such as mantle melting and cooling, and the generation of a magnetic field. When using these models to interpret specific observations of the Earth and other planets, care must be taken in particular for the choice of geometry (see Noack & Tosi, 2012, for an overview of geometries), as this may significantly impact quantities such as the mantle temperature, the convection velocity, and the heat flux of the simulations.

The role of two-dimensional geometry studies in the field of thermochemical mantle convection modeling is still predominant despite an ever-increasing computing power. Although the formulation of 3D grids has seen improvements in previous years with the Yin-Yang grid (Kageyama & Sato, 2004) and the spiral grid (Hüttig & Stemmer, 2008a) among others; simulations with a full spherical shell geometry remain highly expensive in terms of computational power, hence making them inappropriate to study broad ranges of parameters or conduct large exploratory studies. As an alternative, geometrical analogues to the 3D spherical shell have been extensively used, namely the 2D spherical axi-symmetric (van Keken & Yuen, 1995) and the more popular cylindrical geometry (Jarvis, 1993). The 2D axi-symmetric geometry has been used in earlier studies of mantle convection (e.g., van Keken & Yuen, 1995; Jarvis et al., 1995), but in addition to the artificial boundaries formed by the poles which trap down- and up-wellings, an asymmetry between the polar and the equatorial regions exists (van Keken, 2001). The cylindrical geometry on the other hand, while resolving the problems of the artificial boundaries at the poles imposed by the axi-symmetric geometry, still exhibits an important drawback. The ratio of the two surfaces (the planetary surface and the core surface) is different in the cylindrical geometry compared to the spherical shell. This leads to a mismatch in heat flux values between these geometries, as the heat flux of the core mantle boundary (CMB) is underestimated and the surface heat flux is overestimated when comparing to a spherical shell with the same ratio between the core and planet radius (i.e., radius ratio).

In order to mitigate this problem, van Keken (2001) introduced a re-scaling of the 2D cylindrical geometry such that the ratio of outer and inner areas of the cylinder matches the ratio obtained for the spherical shell. This scaling, however, while correcting the surface ratio discrepancy of the cylinder, still uses the volume of a cylinder. Additionally, this re-scaling creates an artificially smaller core, which in turn modifies the convection pattern in the mantle, leading for example to a crowding of the plumes near the CMB, a behavior that would not be observed in a 3D spherical shell, when using the original, non-scaled radii.

To overcome this major drawback of the cylindrical geometry, another 2D geometry called "spherical annulus" has been proposed by Hernlund and Tackley (2008). This geometry effectively uses a second degree of curvature and considers the same surfaces and volumes as the 3D geometry. Since no re-scaling is necessary for this geometry, it keeps the same radius ratio as the 3D one. In the study of Hernlund and Tackley (2008), the spherical annulus showed promising results to approximate the 3D spherical geometry with mean temperature and Nusselt number well reproduced for steady-state thermal convection calculations. While these results a highly valuable, there are only for the case of an Earth-like radius ratio and only consider thermal convection simulations in the Boussinesq approximation.

More recently, Guerrero et al. (2018) performed a more extensive study with the spherical annulus for stagnant lid convection models and compared the temperature distribution between the spherical annulus and the spherical shell. However, an extensive study investigating the ability of the 2D spherical annulus to reproduce results obtained in a 3D spherical shell and a systematic comparison with the 2D cylinder for various setups has never been conducted so far.

In this study, we present simulations of thermal convection in the 2D spherical annulus and compare the results to the 2D cylinder and the 3D spherical shell. In a first part we focus on simple steady-state convection models using the Boussinesq approximation. We vary the Rayleigh number, the radius ratio, and the heating mode for isoviscous cases and run additional temperature-dependent viscosity models to determine which of the two 2D geometries (i.e., cylinder or spherical annulus) is able to best reproduce the 3D results. The set of equations that were used for this comparison are described in Section 2.1, the grid geometries are displayed in Section 2.2, and a description of the cases investigated here is available in Section 2.3. A detailed analysis of the results is presented in Section 2.4.

In a second step, we run more complex simulations of thermal evolution with the same geometries in three separate scenarios. We use Moon-like, Mars-like, and Mercury-like thermal evolution models to investigate how well the 2D spherical annulus reproduces the results of the 3D spherical shell geometry. The three planetary bodies were chosen since they cover a wide range of interior structures and they are all thought to have been in a stagnant lid regime over their entire thermal history, which makes them comparable in terms of their tectonic regime (Breuer & Moore, 2015). In Section 3.1 we list the equations used for the thermal evolution models. A description of the employed parameters and setup of the models is given in Section 3.2. The results are described in Section 3.3. A discussion of the steady-state and thermal evolution models is presented in Section 4, followed by conclusions in Section 5.

2 Steady-state mantle convection

In a first set of calculations we focus on the comparison between steady-state calculations in 2D and 3D geometries. For this purpose we test a large number of parameter combinations for isoviscous models and temperature-dependent viscosity.

2.1 Mathematical model

Fully dynamical models of mantle convection allow us to investigate the spatial and temporal evolution of mantle flow. These models solve the conservation equations of mass, momentum, and energy. Here, the conservation equations are scaled using the mantle thickness D as length scale, the temperature drop across the mantle ΔT as temperature scale and the thermal diffusivity κ as time scale. A Table listing the scaling factors is available in the Supplementary Information, SI (Table S1). By assuming a Newtonian rheology, an infinite Prandtl number, and considering the Boussinesq approximation (Schubert et al., 2001; van Zelst et al., 2022), the non-dimensional conservation equations read:

$$\begin{aligned} \nabla \cdot \mathbf{u} &= 0, && (1)\\ \nabla \cdot \left(\eta \left(\nabla \mathbf{u} + (\nabla \mathbf{u})^T\right)\right) + RaT\mathbf{e}_r - \nabla P &= 0, && (2)\\ \frac{DT}{Dt} - \nabla^2 T - H &= 0. && (3) \end{aligned}$$

In Equations 1 – 3, $\mathbf{u}$ is the velocity vector, η is the viscosity, T is the temperature, $\mathbf{e}_r$ is the radial unit vector, P is the dynamic pressure, and t is the time.

The parameter Ra denotes the thermal Rayleigh number, a non-dimensional number, which controls the vigor of the convection in the mantle. H is the internal heating rate of the mantle that is given by $\frac{Ra_Q}{Ra}$, where Ra_Q denotes the Rayleigh number associated with internal heating. The Rayleigh numbers Ra and Ra_Q read:

$$Ra = \frac{\rho_{ref} g_{ref} \alpha_{ref} \Delta T D^3}{\kappa_{ref} \eta_{ref}}, \quad RaQ = \frac{\rho_{ref}^2 g_{ref} \alpha_{ref} H D^5}{\kappa_{ref} \eta_{ref} k_{ref}}, \tag{4}$$

where ρ_{ref} is the reference density, g_{ref} is the reference gravitational acceleration, α_{ref} is the reference thermal expansivity, κ_{ref} is the reference thermal diffusivity, η_{ref} is the reference viscosity, k_{ref} is the reference thermal conductivity, and H is the internal heating rate in W/kg.

For the steady-state models, we use a constant or temperature-dependent viscosity that follows the Frank-Kamenetskii approximation (Frank-Kamenetskii, 1969), which is a linearized form of the Arrhenius law:

$$\eta(T) = \exp(\Delta\eta_T (T_{ref} - T)), \tag{5}$$

The parameter $\Delta\eta_T$ is the viscosity contrast due to temperature and T_{ref} is the reference temperature at which a non-dimensional viscosity equal to 1 is attained. For the thermal evolution simulations presented further in this study, we use another parametrization of the viscosity (Eq. 9), which is discussed more in-depth in the Section 3.1.

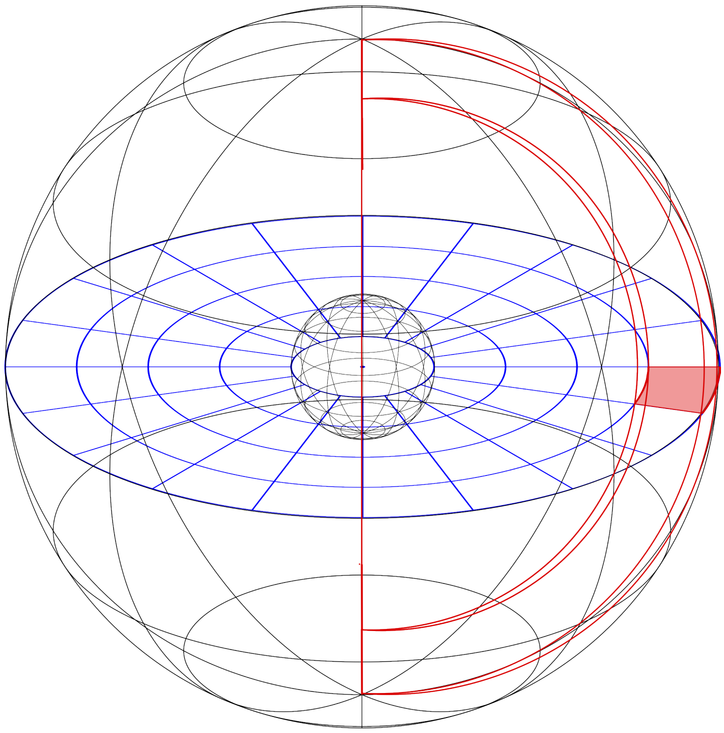

Figure 1: Representation of a cell of the spherical annulus geometry, in red, its effective volume. The cylindrical geometry is represented in blue, on the equatorial plane. The red area represented corresponds to the intersection of the spherical annulus cell with the equatorial plane. When looking at the grid from a polar point of view, its visualization becomes thus indistinguishable from the cylindrical cell.

2.2 Grid geometries

We use the numerical code Gaia (Hüttig & Stemmer, 2008a, 2008b; Hüttig et al., 2013) to model the mantle convection in the interior of rocky planets. Gaia solves the conservation equations (Eq. 1 – 3) in their dimensionless form in 2D and 3D geometries. For the 2D geometry, we use both the classical cylindrical geometry (van Keken, 2001) and the spherical annulus geometry following the approach of Hernlund and Tackley (2008). In the 2D cylindrical geometry, the areas and volumes of the grid cells are typically formulated using the equations for a cylinder; however, what makes the particularity of the spherical annulus geometry, is the addition of a virtual thickness to the cylindrical geometry which varies with the radius r. Thus the spherical annulus has a second degree of curvature, and uses an effective 3-dimensional formulation for the areas and volumes, as represented on Figure 1 (a more detailed description of the spherical annulus geometry is available in Section S3 of the SI).

The 2D cylindrical geometry is scaled according to the scaling introduced by van Keken (2001), where the inner and outer radii of the cylinder grid (i.e., the core radius and the planetary radius, respectively) are changed such that the ratio between the outer and inner areas of the cylinder matches the ratio obtained in a 3D spherical shell geometry. The equations used to correct the inner and outer radii of the cylinder are the following:

$$\frac{r_{oc}}{r_{ic}} = \frac{r_{os}^2}{r_{is}^2}, \qquad\qquad r_{oc} - r_{ic} = r_{os} - r_{is}, \tag{6}$$

where r_{ic} and r_{oc} are the inner and the outer radius of the cylinder, respectively. The inner and outer radii of the spherical shell are denoted by r_{is} and r_{os}, respectively. In the following, we will refer to this type of geometry that considers the rescaling of the inner and outer radii as the "scaled cylinder geometry".

2.3 Case definition

In the first part of this study, we performed steady-state simulations in order to investigate the effects of the ratio of the inner to outer radius and of heating modes on the results obtained with the 2D cylindrical, 2D spherical annulus, and 3D spherical shell geometry. Our aim is to compare 2D and 3D geometries and determine for which scenarios does the 2D spherical annulus give closer results to the 3D compared to the 2D cylinder. To this end, we use models heated from below (purely bottom-heated), from within (purely internally-heated), and from both below and within (mixed heated). We use an initial random perturbation of the temperature field with an amplitude of 5%, vary the Rayleigh number Ra of our simulations from 10^4 up to 10^8, and the radius ratio f from 0.2 to 0.8 for our isoviscous setup.

For the 2D geometries, we use between $1.1{\times}10^4$ and $6.7{\times}10^4$ grid points for low Rayleigh number simulations and between $4.8{\times}10^4$ and $4.1{\times}10^5$ for simulations with a Rayleigh number higher than 10^6. For the 3D geometries, we use between $2.04{\times}10^6$ and $2.94{\times}10^6$ grid points. A more in depth description of each grid and its associated lateral and radial resolution is available in the SI. A short comparison of our results to the ones of Hernlund and Tackley (2008) for isoviscous steady-state cases is presented in Section S4 of the SI.

Each mesh has a prescribed temperature and free-slip velocity as boundary conditions. The temperature of the upper boundary T_{surf} is set to zero, while the one of the lower boundary is set to one for the bottom heated and mixed heated cases. For the purely internally heated cases we use a zero heat flux at the core-mantle boundary.

The simulations are ran until a statistical steady-state is reached. Then, output quantities such as the average temperature, root-mean-square velocity, and top temperature gradient are computed using an average over the last 10% of the simulation. While for purely steady-state models this is the same as taking the last output, for quasi steady-state time-dependent or periodic models this ensures to retrieve representative average values. The top temperature gradient here is the temperature gradient at the top of the domain, calculated between the last two shells of the grid.

An additional, more complex set of simulations includes the effect of the temperature dependence of the viscosity, and leads to the formation of a stagnant lid at the top of the convecting domain. These simulation represent simplified Moon-like ($f = 0.2$), Mars-like ($f = 0.5$), and Mercury-like ($f = 0.8$) scenarios. We use here thermal and radiogenic Ra numbers with values similar to those expected for planetary mantles, i.e., $Ra = 5 \times 10^6$ and $Ra_Q = 5 \times 10^7$ (see values of Ra and Ra_Q in Table 1). We use the Frank Kamenetskii parametrization for the viscosity (Eq. 5) and set a viscosity contrast $\Delta\eta_T$ to 10^8 at a reference temperature T_{ref} of 0.5 to ensure that we are in a stagnant lid convection regime. In this setup, the total number of nodes used for the 2D grids lies between $4.8{\times}10^4$ and $2.8{\times}10^5$; while for the 3D simulations, the total number of nodes is 2.9×10^6.

In total, we run 180 isoviscous simulations and 36 temperature-dependent viscosity cases. All parameters and the grid resolutions for these steady-state simulations are listed in Table S2 in the SI.

2.4 Results

2.4.1 Isoviscous convection

For the first set, consisting of isoviscous simulations, we provide a thorough and systematic comparison between the 3D spherical grid and the two 2D geometries, namely the spherical annulus and the cylindrical geometry. A summary of the comparison is shown in Figure 2.

Here, the analysis of the 180 simulations has been summarized into three subplots one for each heating mode. Each subplot contains two rows showing for each the annulus geometry (first row) and the scaled cylindrical geometry (second row), respectively, the relative error to the 3D results. The computation details of the relative error can be found in the SI (Section S5) along with tables containing the values for each simulation in CSV format. Figure 2 shows that the mean domain temperature of the 3D geometry is more accurately reproduced by the spherical annulus geometry than by the cylindrical one in every heating mode, up to values of $Ra = 10^7$. This difference is even more noticeable in the low radius ratiosetups (i.e., $f = 0.2$ and 0.4), which can be seen for the purely bottom heated and mixed heated scenarios. We also see for the purely internal heated cases and high Rayleigh number cases (i.e., $Ra = 10^7$ and $Ra = 10^8$) that this difference is even more dramatic with an overestimation of the temperature in the cylindrical geometry by up to $\sim 20\%$ for the small a radius ratio (i.e., $f = 2$) and reduces to only a few percent in the spherical annulus.

In the case of the root mean square velocity, we see a general increase of the accuracy with the spherical annulus geometry, however this increase is less pronounced than what is observed for the mean temperature. We see a slightly better match for the purely bottom heated and mixed heated setups, where simulations with $Ra < 10^7$ go from being slightly underestimated by the cylinder to slightly overestimated by the annulus. However, the cases with $Ra \geq 10^7$ show a net improvement, with an underestimation decreasing for all the cases with a radius ratio higher than 0.2. For the setup with a purely internal heating, however, almost no improvement is visible, with the notable exception of the simulation with a $Ra = 10^8$ and a radius ratio of 0.2 being overestimated by $\sim$ 40% in the case of the cylinder, which turns to be overestimated only by $\sim 20\%$ in the case of the spherical annulus.

In comparison to the cylinder, the spherical annulus, gives less conclusive results for the top temperature gradient. We can see an improvement in case of small radius ratios (i.e., $f = 0.2$) with either purely internal heating or mixed heating, or in the case of high Rayleigh numbers (i.e., $Ra \geq 10^7$) for purely internal heated cases. Otherwise, for the majority of the setups and heating modes, the spherical annulus does not show significant improvement in reproducing the 3D values compared to the scaled cylindrical geometry. A comparison of the temperature gradient at the top of the mantle shows that the spherical annulus is hardly able to reproduce the 3D values more accurately than the scaled cylindrical geometry, with the notable exception of low radius ratios of around $f = 0.2$.

2.4.2 Stagnant lid convection

In the second part of the steady-state simulations, we modeled stagnant lid convection while varying the heating mode, the radius ratio, and the geometry in order to study the accuracy of the spherical annulus geometry (see SI, Table S2). In this type of setup, where the viscosity is strongly dependent on temperature, the convection is expected to operate in a stagnant lid regime. This rigid layer that forms at the top of the domain restricts convective heat transfer to the deep interior.

The results are summarized in Figure 3, where we report the relative error of the 2D cylindrical, 2D scaled cylindrical, and 2D spherical annulus geometry to the 3D spherical shell. Here we inspect the mean temperature, the root mean square velocity, the top

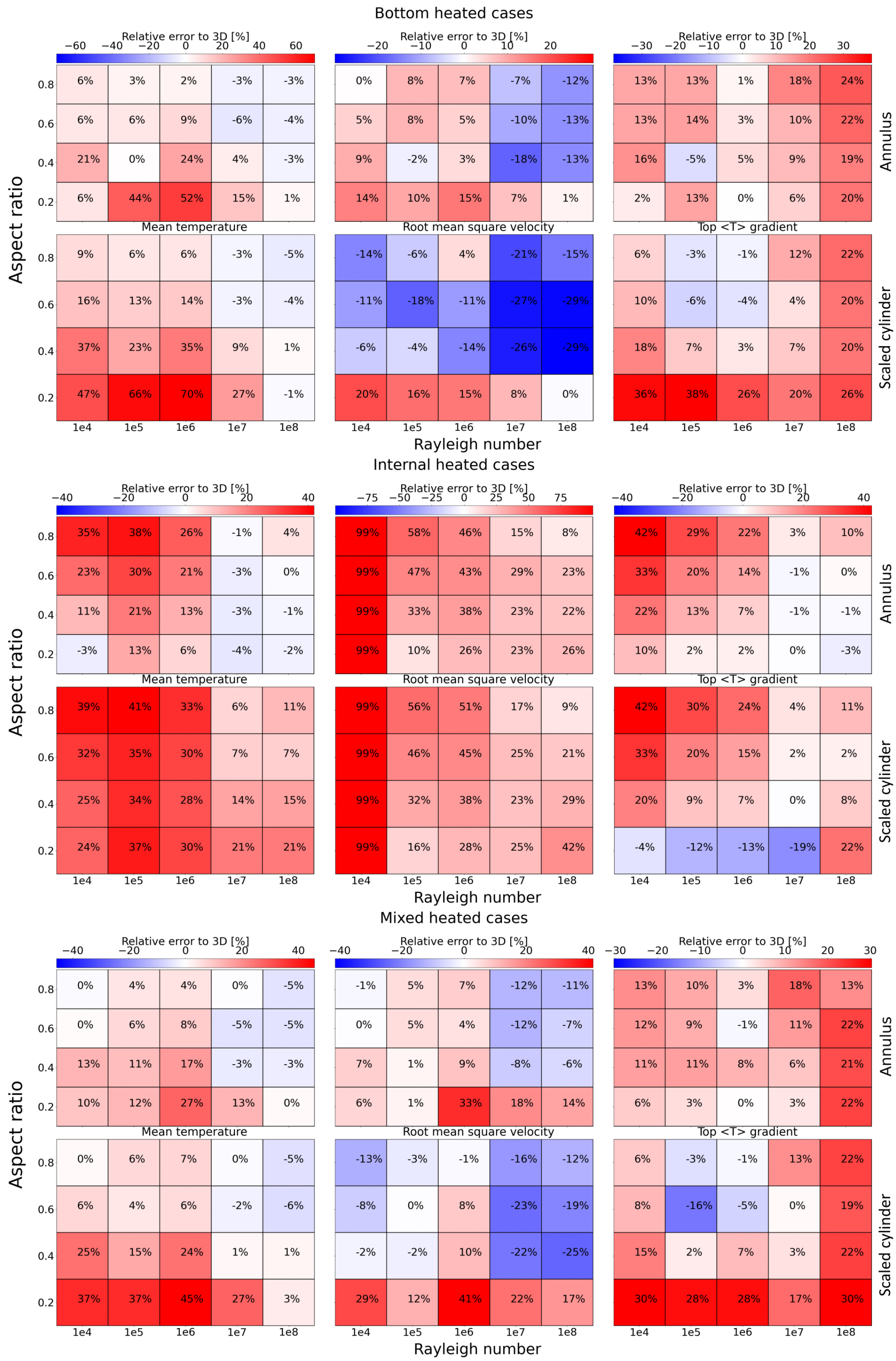

Figure 2: Averaged computed relative error to the 3D geometry with 3 different heating modes, i.e., purely basal heated (top row), purely internal heated (middle row), or mixed heated (bottom row) for steady-state isoviscous convection simulations. For each heating mode the first line of plots shows the relative errors for the spherical annulus and the second line represents the scaled cylinder. The thermal Rayleigh number and internal Rayleigh number vary from 10^4 to 10^8 and the radius ratio from 0.2 to 0.8. The radius ratio indicated on the plot is the one corresponding to the reference 3D simulations. In the case of the cylinder, the radius ratio is scaled, thus a 0.2 radius ratio becomes 0.04 following the scaling formula from van Keken (2001) (eq. 6). For columns from left to right, relative error of the mean temperature, of the v_{rms}, and of the top temperature gradient are shown.

temperature gradient, and the stagnant lid thickness. For each simulation we use a Ra of 10×10^6 and Ra_Q of 10×10^7.

In Figure 3, when considering purely basal heating, we see that the spherical annulus is overall better at reproducing the 3D values compared to the scaled and non-scaled cylinder. The highest discrepancy is observed for the radius ratio $f = 0.2$, with $> 50\%$ of overestimation on average for the 2D geometries. For the spherical annulus, the mean temperature matches best the one of the 3D spherical shell when the radius ratio increases, an effect also seen for the $\mathrm{v_{rms}}$. The top temperature gradient does not follow this pattern, however, while the stagnant lid error is the lowest for $f = 0.5$. The highest difference to the 3D for the low radius ratio setups ($f = 0.2$) in the purely bottom heated setup that we found in our models is in agreement with Guerrero et al. (2018). The study by Guerrero et al. (2018) considered stagnant lid convection with only basal heating, and observed that for small radius ratio setups, the spherical annulus would systematically show a hotter temperature when compared to the 3D. This behavior is indeed confirmed by our simulations, where we can observe that the different geometry of plumes between the spherical annulus and the spherical shell create considerable differences in temperature in the low radius ratio and bottom heated simulations. Plumes in a 2D geometry are rather sheet-like than column-like as they are in a 3D geometry. This leads to a warmer temperature in the 2D geometries compared to the 3D as being the consequence of a topological difference between flows in a spherical shell and spherical annulus, as explained by Guerrero et al. (2018). Moreover, this difference is strongly accentuated for low radius ratios, where the number of plumes is small and such geometrical effects significantly affect the results. For a better illustration of this behavior we refer the reader to Figure S5 of the SI. The increase of temperature differences with increasing f was also observed by Guerrero et al. (2018) and is confirmed by our results.

In the case of a purely internally heated case, we see that the annulus fares remarkably better than the cylindrical geometries and that the average relative error of the mean temperature, the $\mathrm{v_{rms}}$, and top temperature gradient diminish as the radius ratio decreases. The highest radius ratio (i.e., $f = 0.8$) shows here the highest discrepancy between 2D and 3D, with more than 50% and 20% of overestimation for the v_{rms} and the top temperature gradient respectively, while the stagnant lid is underestimated on average by 15%. When taking a closer look at the simulations, it appears that, the internal heating simulations in 2D have a tendency to require more convective strength in order to transport the same amount of heat in the domain compared to a 3D simulation, as already shown in Hernlund and Tackley (2008). This peculiarity when investigating the temperature and velocity distribution will apparently create a larger amount of downwellings in the case of a 3D model for a given internal heating rate when compared to a 2D one. This can be seen on the Figure S7 of the SI.

For cases heated both from below and from within (i.e., mixed heated cases), the spherical annulus is showing the best results for the mean temperature, the top temperature gradient, and the stagnant lid thickness when the radius ratio is the lowest (i.e., $f = 0.2$). For the highest radius ratio considered here (i.e., $f = 0.8$), the results obtained with the spherical annulus and the cylinder geometries show similar errors, with the exception of v_{rms} that seems to be best reproduced by the scaled cylinder geometry.

When combining purely basal heating with internal heating, the main discrepancy previously arising from the low radius ratio and purely basal heated simulations seems to be mitigated by the addition of internal heating. The difference in the temperature distribution between the spherical annulus and the spherical shell tends to disappear (see Figure S7 of the SI).

In summary, for the stagnant lid cases presented here, the mean temperature is overall better reproduced by the spherical annulus independently of the radius ratio or heating mode. Additionally, in the intermediate to low radius ratio simulations ($f \leq 0.5$), the spherical annulus can also reproduce the 3D velocities, the top temperature gradient, and the stagnant lid better than the cylinder geometry.

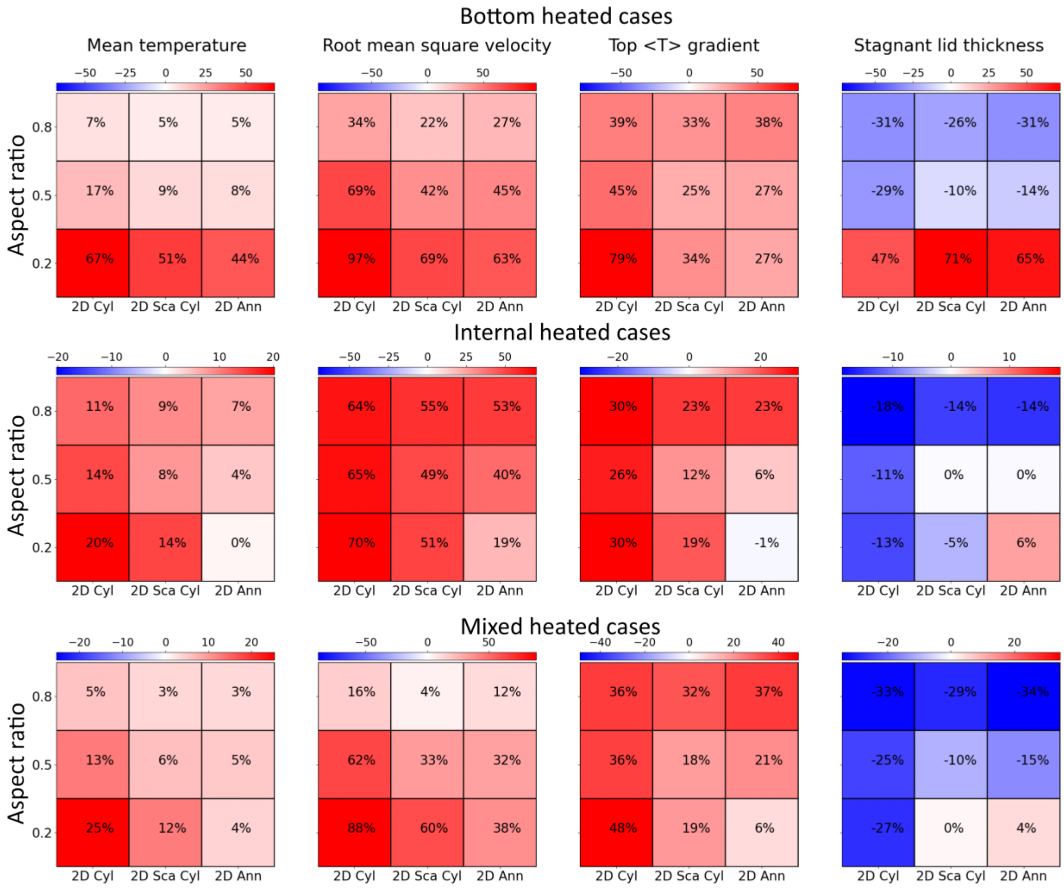

Figure 3: Averaged computed relative error to the 3D geometry with 3 different heating modes (i.e., purely basal heated, purely internal heated, and mixed heated) for steady-state convection simulations with a temperature dependent viscosity. The mean temperature of the domain, the root mean square velocity, the temperature gradient at the top of the domain, and the stagnant lid thickness are compared here. For each subplot analyzing the relative error in a given heating mode, every column represents a different geometry, namely the 2D cylinder, the 2D scaled cylinder, and the 2D spherical annulus. The thermal Rayleigh number is 5×10^6, the internal Rayleigh number is 5×10^7, and the investigated radius ratios are 0.2, 0.5, and 0.8.

3 Thermal evolution models

In this part we compare the 2D and 3D geometries in a more complex set-up, by using thermal evolution models in a stagnant lid regime. Compared to the previously discussed steady-state calculations, these models illustrate which of the 2D geometries can best reproduce the 3D results when mantle and core cooling are considered.

3.1 Mathematical model

For the thermal evolution models we use the Extended Boussinesq Approximation (EBA) (Schubert et al., 2001) to account for adiabatic heating and cooling. The energy equation (Eq. 3) becomes:

$$\frac{DT}{Dt} - \nabla \cdot (k\nabla T) - Di\alpha(T + T_{surf})\mathbf{u}_r - \frac{Di}{Ra}\Phi - H = 0, \tag{7}$$

where $\mathbf{u}_r$ is the radial component of the velocity vector, T_{surf} is the surface temperature, α is the thermal expansivity, and Φ is the viscous dissipation given by $\Phi = \tau : \dot{\varepsilon}/2$, where τ is the deviatoric stress tensor and $\dot{\varepsilon}$ the strain rate tensor. The dissipation number Di is defined as follows:

$$Di = \frac{\alpha_{ref} g_{ref} D}{c_p}, \tag{8}$$

where c_p is the mantle heat capacity.

In the thermal evolution models, we consider a temperature and pressure dependent viscosity that follows the Arrehnius law of diffusion creep. The non-dimensional equation for viscosity reads (Roberts & Zhong, 2006):

$$\eta(T, z) = exp\left(\frac{E + zV}{T + T_{surf}} - \frac{E + z_{ref}V}{T_{ref} + T_{surf}}\right), \tag{9}$$

where E and V are the activation energy and the activation volume respectively (Karato & Wu, 1993; Hirth & Kohlstedt, 2003). T_{ref} and z_{ref} are the reference temperature and depth, respectively, at which the reference viscosity is attained. The non-dimensional T_{ref} and z_{ref} values correspond to a dimensional reference temperature of 1600 K and a dimensional reference pressure of 3 GPa, respectively.

The temperature of the lower boundary T_{CMB} evolves following a 1-D energy balance, assuming a core with constant density and heat capacity (Stevenson et al., 1983):

$$c_c \rho_c V_c \frac{dT_{CMB}}{dt} = -q_c A_c, \tag{10}$$

where c_c is the heat capacity of the core, ρ_c is the core density, V_c is the core volume, q_c is the heat flux at the core-mantle boundary (CMB), and A_c is the core surface area. Here we do not consider core crystallization.

As appropriate for thermal evolution models, we take into account the decay of the heat producing elements (i.e., Ur^{238}, Ur^{235}, Th^{232}, and K^{40}). The amount of radioactive heat sources is calculated using the concentrations listed in Table 1.

In thermal evolution models we consider the effect of a 50 km laterally homogeneous crust. This crust is enriched in radiogenic elements while the mantle is depleted according to the following mass balance:

$$M_{tot} \cdot Q_{tot} = M_{mantle} \cdot Q_{mantle} + M_{crust} \cdot Q_{crust}, \tag{11}$$

where M is the mass and Q is the heating rate. This setup also considers the blanketing effect of the crust by using a lower thermal conductivity k in the crust compared to the mantle.

3.2 Case definition

We test three scenarios for the thermal evolution of a Mars-like, the Moon-like, and Mercury-like planet. We model the entire evolution of these planets to determine the variations over time of several key output quantities. These three planetary bodies were chosen because of their different interior structures. In the Mars-like case, the radius ratio between core and planetary radius is $f = 0.544$. The Moon- and Mercury-like scenarios represent two end-members in terms of their radius ratios, with $f = 0.224$ and $f = 0.828$, respectively.

In the case of the 2D grids, we use a radial resolution of ~ 10 km for Mars- and Moon-like cases, and a ~ 5 km radial resolution for the thin mantle of Mercury. In the case of the 3D grids, the radial resolution lies between 22 and 9 km, and we use a lateral resolution of 40962 points per shell. A more detailed list of the resolution for every grid is available in Table S2 of the SI.

In the cylindrical geometry, we use both the classical cylinder and the rescaling of van Keken (2001) as done previously in the stagnant lid steady-state simulations. It is worth to note that for the peculiar Moon-like interior structure, the scaling of the respective radii leads to a radius ratio $f = 0.0503$. Since this is an extreme case, we test whether the rescaling of the cylinder geometry is appropriate for such interior structures in a thermal evolution scenario.

It is important to note here that for each planet we use different Rayleigh numbers (i.e., Ra and Ra_Q). These are calculated self-consistently using the mantle thickness, internal heat sources, and temperature difference accross the mantle specific for each planet. The parameters are listed in Table 1. While for Mars- and Moon-like simulations we use a reference viscosity of 10^{21} Pa s, for the Mercury-like case we perform additional tests with a reference viscosity that is lower by two orders of magnitude (i.e., 10^{19} Pa s). Since the thin Mercurian mantle typically leads to a conductive state after a few Gyr of evolution, by using a lower reference viscosity we test additional scenarios, in which convection can be sustained over most of the evolution. The results for Mercury with $\eta_{ref} = 10^{21}$ Pa s and 10^{19} Pa s are also compared between the 3D spherical shell and the 2D geometries.

In all our simulations we consider the presence of a primordial crust with a thickness of 50 km, which is enriched in radiogenic elements compared to the bulk heat sources of the planet by a factor of 2 and has a two times lower thermal conductivity than the mantle (see Table 1). While being a representative value for the enrichment of the Mercurian crust (Tosi, Grott, et al., 2013), for the two other scenario it allows to increase the complexity of the simulation without having a thermal evolution dominated by the enrichment of the crust. A second set of thermal evolution models neglecting the effects of the crust is listed in Section S7 of the SI.

3.3 Results

In the following, we present the results obtained for the thermal history of Mars, the Moon, and Mercury for all geometries. Similar to the steady-state calculations, we show in Figure 3 the difference of the 2D cylinder, 2D scaled cylinder, and 2D spherical annulus to the 3D results after 4.5 Gyr of evolution (i.e., at present day). In addition to the error shown in percent, we also list the difference between the dimensional values for mean temperature, CMB temperature, root mean square velocity, lid thickness, as well as surface and CMB heat fluxes (Figure 4).

Figure 5 shows the entire evolution over 4.5 Gyr of the output quantities of interest for all four geometries (2D cylinder, 2D scaled cylinder, 2D spherical annulus, and 3D spherical shell) for a Mars-like geometry. Our results show clearly that in the case of a Mars-like geometry, the values obtained during the entire thermal evolution with

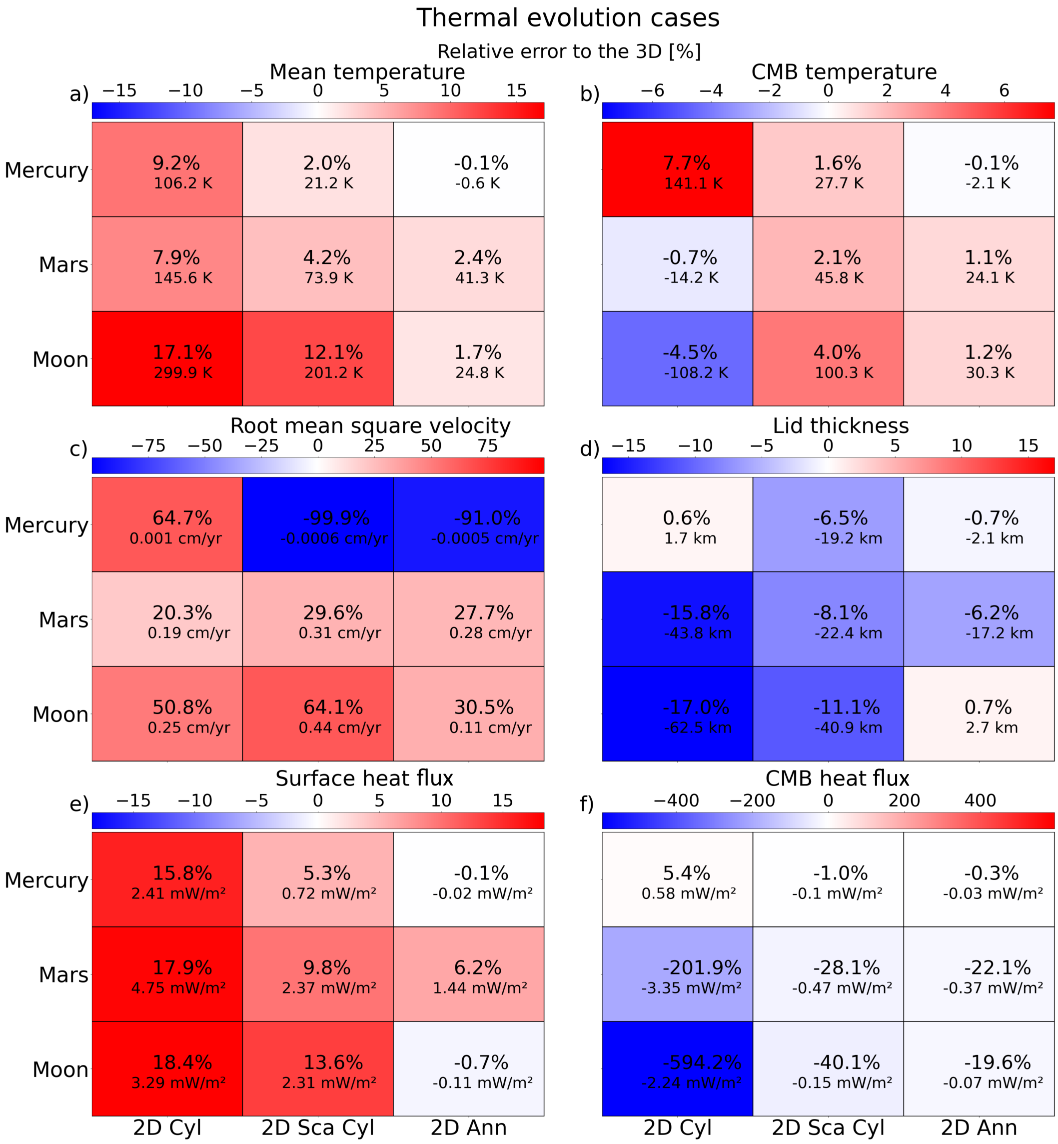

Figure 4: Relative error to the 3D in the case of thermal evolution simulations. In each panel we vary the planet on the y axis and on the x axis we vary the geometry. We investigate the relative error for: the mean temperature (a), the CMB temperature (b), the root mean square velocity (c), the stagnant lid thickness (d), the surface heat flux (e), and the CMB heat flux (f). A color in the blue indicates an underestimation of the results obtained in the 3D geometry whereas a color in the red indicates an overestimation. 2D Cyl stands for non-scaled 2D cylindrical geometry, 2D Sca Cyl is 2D cylindrical geometry with the scaling by van Keken (2001), and 2D Ann stands for 2D spherical annulus geometry. Each panel shows the relative error in % to the 3D and the absolute error in dimensional unit.

Symbol	Description (Unit)	Mars	Moon	Mercury
R_p	Planetary radius (km)	3400	1740	2440
R_c	Core radius (km)	1850	390	2020
D	Mantle thickness (km)	1550	1350	420
f	Radius ratio (-)	0.544	0.224	0.827
T_{surf}	Surface temperature (K)	220	250	440
T_{CMB}	CMB temperature (K)	2000	2000	2000
T_{ref}	Reference temperature (K)	1600	1600	1600
ΔT	Temperature contrast across the mantle (K)	1780	1750	1560
g	Gravitational acceleration ($m.s^{-2}$)	3.7	1.6	3.7
η_{ref}	Reference viscosity (Pas)	10^{21}	10^{21}	10^{21}
κ	Thermal diffusivity (m^2/s)	1×10^{-6}	1.06×10^{-6}	1.04×10^{-6}
α	Thermal expansivity (K^-1)	2.50×10^{-5}	2.50×10^{-5}	2.50×10^{-5}
Ra	Rayleigh number(-)	2.14×10^6	5.35×10^5	3.49×10^4
RaQ	Internal heating Rayleigh number (-)	5.91×10^7	8.70×10^6	8.00×10^4
ρ_{core}	Core density (kg/m^3)	6000	7500	6980
ρ_{mantle}	Mantle density (kg/m^3)	3500	3300	3380
ρ_{crust}	Crust density (kg/m^3)	2900	2700	2900
$c_{p,m}$	Mantle heat capacity (kgK)	1142	1142	1142
$c_{p,c}$	Core heat capacity (kgK)	850	850	850
V	Activation volume (m^3/mol)	6.00×10^{-6}	6.00×10^{-6}	6.00×10^{-6}
E	Activation energy (J/mol)	3.00×10^5	3.00×10^5	3.00×10^5
k_m	Mantle thermal conductivity ($Wm^{-1}K^{-1}$)	4	4	4
k_{cr}	Crust thermal conductivity ($Wm^{-1}K^{-1}$)	3	2	3
D_{crust}	Primordial crust thickness (km)	50	50	50
	Heat source concentration	(Taylor, 2013)	(Taylor, 1982)	(Padovan et al., 2017)
C_U	Uranium concentration (ppb)	16	33	7
C_{Th}	Thorium concentration (ppb)	58	125	29
C_K	Potassium concentration (ppm)	309	83	550

Table 1: Parameters for thermal evolution calculations for Mars, Moon, and Mercury. Note that the non-dimensional radii are rescaled according to Eq. 6 for the scaled cylinder geometry.

a 3D geometry are more closely reproduced by the spherical annulus than the cylinder, irrespective of whether it is scaled or not. It is to note that the spherical annulus geometry is reproducing especially well the evolution of the mean and core-mantle boundary temperatures (see Figure 4 for the actual present-day error), while the velocities are systematically overestimated by the 2D geometries (27.7% for the spherical annulus and 29.6% for the rescaled cylinder). This directly affects the calculation of the stagnant lid thickness, and thus underestimates it by 6.2% for the annulus and 8.1% for the rescaled cylinder. When trying to reproduce the heat fluxes at present day, the spherical annulus is somewhat better than the scaled cylinder, with an approximated underestimation of the CMB heat flux by 22% compared to 28% for the scaled cylinder, while the surface heat flux will be overestimated by 6% and 8% for the annulus and the scaled cylinder, respectively. While we focus in this part mostly on present-day values, when examining the entire thermal evolution of the planet we observe in the early and middle stages (between 1 and 3 Gyr) a relative error even larger as the one observed at present day, as seen on Figure 5c and e. The Mars-like setup is the most challenging setup to reproduce for the spherical annulus, and although exhibiting relatively low errors, it still shows the highest discrepancies between the thermal evolution cases with different interior structures. The overestimation of the mean temperature, mean velocity, surface heat flow, and underestimation of the stagnant lid thickness can be linked directly to the mixed heated, temperature-dependent viscosity simulation with a radius ratio of 0.5, which shows the same type of relative error (see Figure 3)

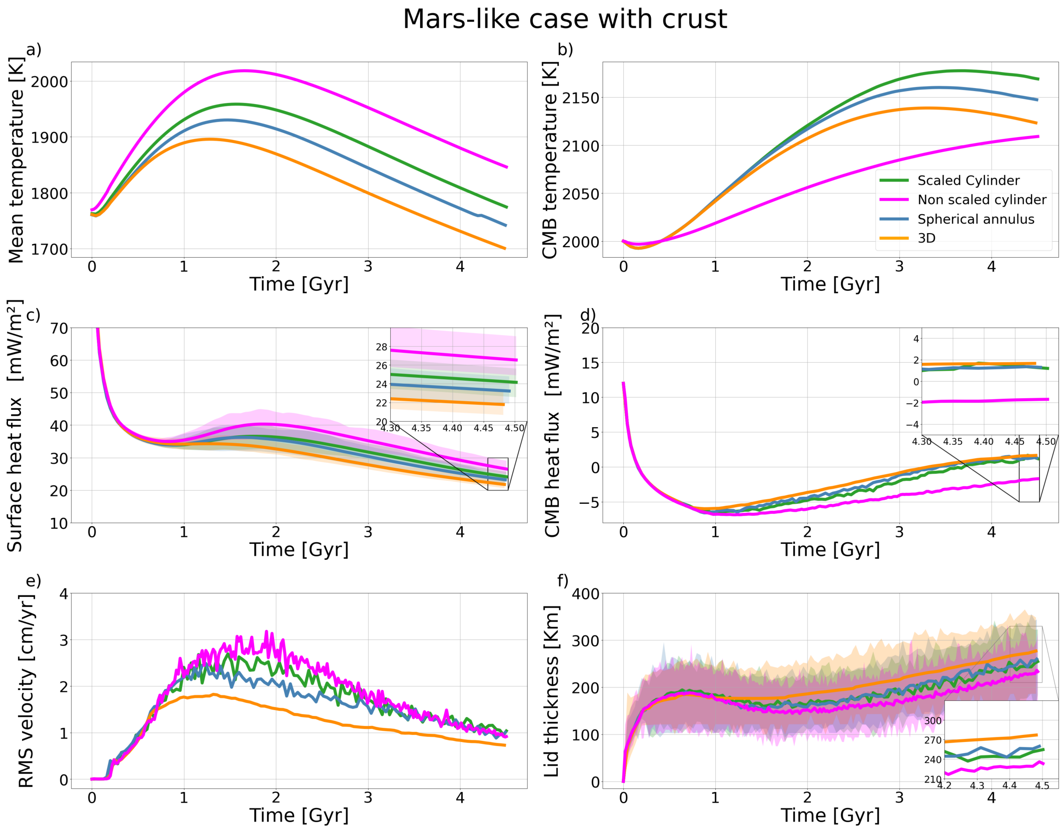

Figure 5: Timeseries of a Mars-like case with an initial crust of 50 km and with 4 different geometries (2D non-scaled cylindrical, 2D cylindrical, 2D spherical annulus and 3D spherical shell). The values shown here are the mean temperature (a), the core-mantle boundary temperature (b), the surface heat flux (c), the core-mantle boundary heat flux (d), the averaged root mean square velocity of the domain (e), and the lid thickness (f) from 4.5 Gyr ago to present day, respectively. The shaded areas show the min.-max. variations during the evolution. The non-scaled cylinder has been added to show the effect of the rescaling introduced by van Keken (2001).

In the case of a Moon-like setup (Figure 6) the differences between the spherical annulus and the cylinder are typically larger than in the Mars-like case. However the difference between the spherical annulus and the 3D is significantly lower in the case of the mean temperature, the stagnant lid thickness and the surface heat flow; as can be seen on Figures 6a, c, and f. The temperatures through time are very well reproduced by the spherical annulus (less than 2% of error compared to more than 12% for the cylindrical geometries). Similarly, the surface heat flux and the stagnant-lid thickness show a good match between the spherical annulus and the 3D geometries (see Table S5 of the SI). Concerning the cylindrical geometries, the effects of the rescaling are plainly visible on the overall temperatures and heat fluxes evolution. As van Keken (2001) showed, the cylinder tends to overestimate the relative importance of the CMB radius compared to planetary radius and requires a rescaling of the radii. However, for the very low aspect-ratio of the lunar mantle, even when the rescaling is applied the results are still largely different compared to a 3D spherical shell geometry. A better approximation of the 3D results is obtained by the spherical annulus, where such rescaling is not needed. We see that the CMB heat flux stays at around -1.86 $\mathrm{mW\,m^{-2}}$ even at present day, meaning that the core is actively heated by the mantle, although in the other geometries the core is already cooling (see Figure 6b and d), a behavior which is also seen for Mars with the non-scaled cylindrical geometry. Similar to what has been seen previously for the low aspect-ratio cases with temperature-dependent viscosity combining basal heating and internal heating (see Figure 3), the scaled and non-scaled cylindrical geometries show large disagreements in all studied metrics. Nevertheless, even in the spherical annulus, the mean velocity and the CMB heat flux present the largest errors among the investigated quantities.

In Figure 7, we show the results of the thermal evolution for a Mercury-like setup. Here we used two sets of simulations in order to illustrate the case of a initially weakly convecting mantle with a reference viscosity set as $\eta_{ref} = 10^{21}$ Pa s resulting in a Rayleigh number of $Ra = 3.49 \times 10^4$; and the case of a mantle presenting a stronger initial convection with a reference viscosity lowered by two orders of magnitude, thus increasing the Rayleigh number to $Ra = 3.49 \times 10^6$. Here again the global trend previously seen for Mars and the Moon emerges. As shown in figure 4, the spherical annulus geometry again reproduces best the 3D results with an approximate error of less than 1%, with a notable exception for the velocities, which are highly overestimated (more than 90% of relative error). The very high relative error of the v_{rms} is explained by the present-day state of the Mercurian mantle. In our simulations, a Mercury-like planet falls into a quasi-conductive state after a couple of Gyr of evolution irrespective of the geometry (Figure 7), which in turn gives very low absolute v_{rms} values. Yet the absolute difference of velocity between the geometry is very small (less than 1×10^3 cm/year). Despite these high relative error values in the velocities, the stagnant lid thickness is, however, quite well reproduced by the 2D geometries, giving a maximum relative error of 19 km (or an underestimation of 6.5%).

4 Discussion

Our results show that the spherical annulus can reproduce the 3D spherical shell geometry better than the cylindrical geometry, consistent with previous studies by Hernlund and Tackley (2008). Our systematic study, using simulations of increasing complexity, shows for the first time in great detail the difference in using a 2D geometry instead of a more realistic 3D spherical shell domain when modeling thermal convection in planetary mantles.

When using the cylindrical geometry, whether scaled or not, the results show substantial differences to the 3D geometry results in steady-state and thermal evolution simulations. The necessity of choosing between a scaled and a non-scaled cylinder in modeling geodynamic processes inevitably results in a trade-off between an accurate repre-

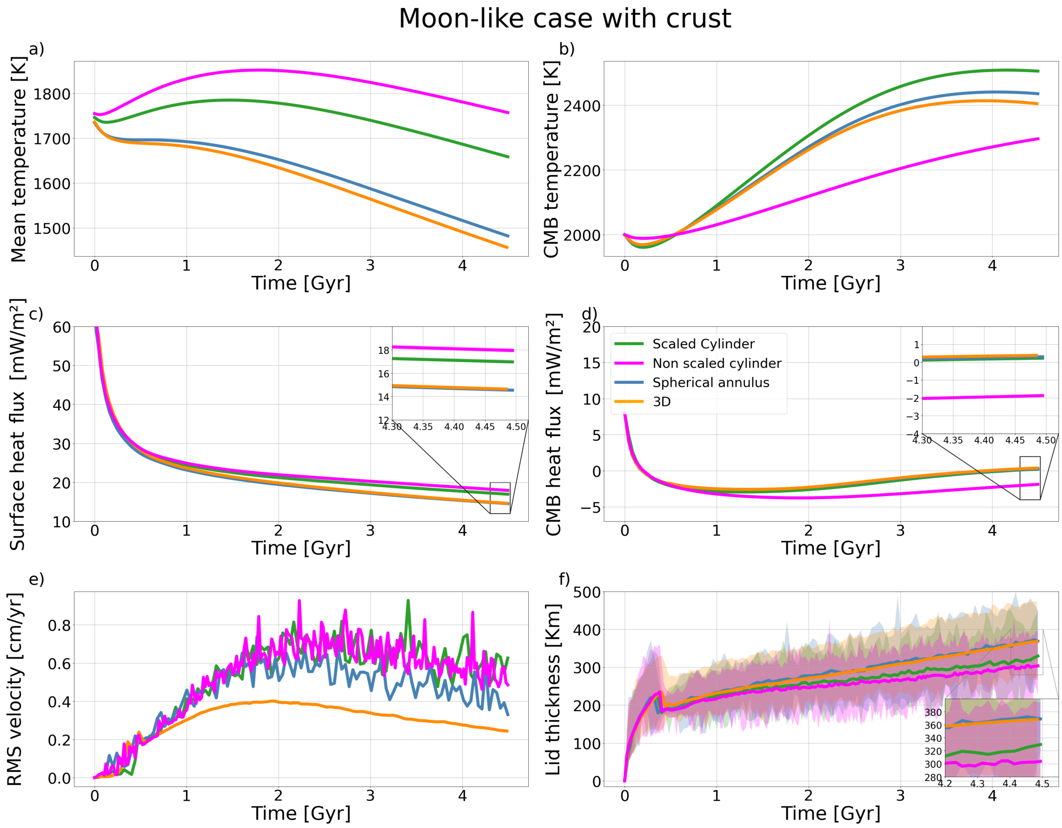

Figure 6: Timeseries of a Moon-like case with an initial crust of 50 km and with 4 different geometries (2D non-scaled cylindrical, 2D scaled cylindrical, 2D non-scaled cylindrical, 2D spherical annulus and 3D spherical shell). For a description off the values investigated, see Figure 5.

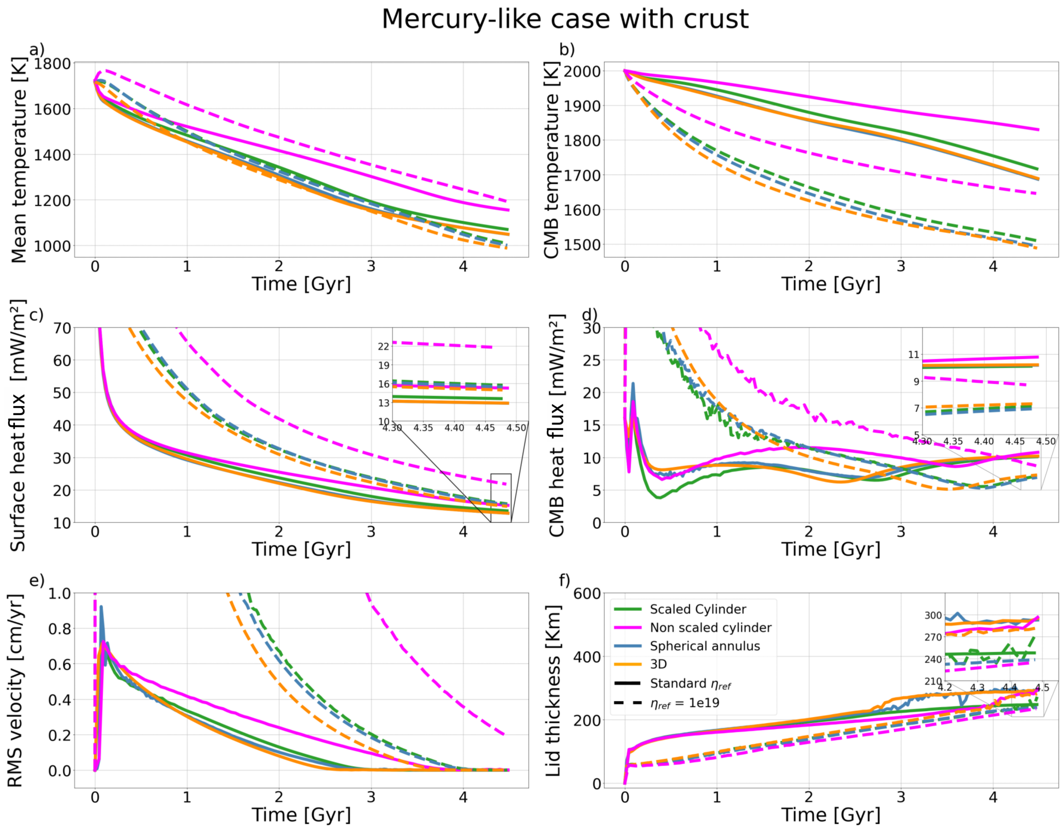

Figure 7: Timeseries of a Mercury-like case with an initial crust of 50 km, with 4 different geometries and 2 different reference viscosities. For a description off the values investigated, see Figure 5. The dotted lines represent simulations with a reference viscosity of η_{ref}=10^{19} Pa s while the solid lines represent the cases with a reference viscosity of η_{ref}=10^{21} Pa s. The maximum and minimum of the output quantities are not displayed here, since these variations are negligible.

sentation of the deep interior structures in the case of the non-scaled cylinder, especially important when studying thermochemical structures (Stegman et al., 2003; Nakagawa & Tackley, 2004; Yu et al., 2019; Kameyama, 2022), and a correct representation of the heat fluxes as well as root mean square velocity in the domain (Deschamps et al., 2010; Mulyukova et al., 2015) for the scaled one. To circumvent these inaccuracies, the systematic use of the spherical annulus in reproducing thermochemical convection in 3D is thus strongly recommended.

In the case of steady-state simulations, we showed that the spherical annulus has the largest error in the high radius ratio scenarios (i.e, $f = 0.6$ and 0.8). The efficiency of the spherical annulus in reducing the error to the 3D (compared to the results of the scaled cylinder) is most visible in the case of a low radius ratio configuration (i.e., $f = 0.2$), while nonetheless displaying large discrepancies in the mean temperature in the case of bottom heated and temperature-dependent setups, as also seen by Guerrero et al. (2018).

Concerning the heating modes, as reported by Hernlund and Tackley (2008), the purely internally heated cases show the largest difference between the 2D and 3D geometries, while the mixed heating cases (bottom and internal heating) tends to be the heating mode for which the spherical annulus exhibits the smallest errors in comparison to the spherical shell, as the difference in the temperature distribution between the spherical annulus and the spherical shell tends to disappear (see Figure S6 of the SI). This particularity becomes quite useful when trying to model more realistic processes such as thermal evolution models of terrestrial planets, as the silicate mantles of planets will invariably show heating induced by both the presence of radiogenic elements in the mantle and by the core. The smaller error between the 2D spherical annulus and 3D spherical shell observed in mixed heated cases makes the spherical annulus an acceptable alternative to model more complex scenario (Figure 4), for which a 3D geometry is too expensive. The trend of the relative error in the steady-state stagnant lid simulations with mixed heating is also observed in the case of thermal evolution models: the errors in the surface heat flux and stagnant lid thickness increase with increasing radius ratio (cf. the errors obtained for the Moon and Mars in Figure 4). However in the case of Mercury, while the steady-state simulations would predict the largest errors, the low Rayleigh number in thermal evolution models and the transition to a conductive state during the thermal evolution strongly reduce the discrepancy between 2D and 3D geometries.

The results presented here show that the spherical annulus is to be preferred to the cylindrical geometry, whether for steady-state simulations or thermal evolution simulations. However, in the case of the thermal evolution simulations one should question whether this geometry is sufficient to approximate the 3D spherical shell. Some observables such as the heat flux, the mechanical thickness of the lithosphere and the crust produced by partial melting of the mantle are used to evaluate the thermochemical evolution of a planet. But an important question is whether the 2D spherical annulus is accurate enough to reproduce the results of a 3D spherical shell for the above mentioned quantities, and which of these observables can be affected the most.

Additional post-processing has thus been conducted in order to better characterize the differences of more complex processes in the spherical annulus compared to the spherical shell. We exclude from this comparison the cylindrical geometry given its lack of accuracy in reproducing 3D. Moreover, the areas and volumes in the 2D cylindrical geometry are truly 2D and thus difficult to compare to the 3D spherical shell. Melting in the mantle, the thickness of the mechanical lithosphere, and heat fluxes are shown in Figure 8 as a function of time. For the calculation of the mechanical lithosphere thickness, we follow the approach of Grott and Breuer (2008). The calculations involving partial melting of the mantle are highly simplified and do not include the effects of latent heat or mantle depletion. While the quantities presented in Figure 8 are based on simple post-processing of the thermal evolution results, they are meant to provide first order implications for the thermal evolution modeling with 2D and 3D geometries (for additional information concerning the post processing, see S11, S12).

When reproducing 3D simulations, the spherical annulus is well suited to replicate melting, mechanical thickness and heat fluxes. In particular the heat fluxes, and especially the CMB heat flux (Figure 8g, h, i) are especially well reproduced in terms of values and trend of evolution. The largest errors were observed for a Mars-like structure with an overestimation of less than 1.5 $\mathrm{mW\,m^{-2}}$ compared to the 3D for the surface heat flux and an almost identical CMB heat flux (less than 1 $\mathrm{mW\,m^{-2}}$ lower values compared to the 3D case).

The mechanical thickness for a Moon-like interior structure will be underestimated on average by 5% for the spherical annulus, while the amount of melting will be overestimated by 10% as in the case of Mercury. Since the computation of the amount of partial melting in the mantle through time relies on the temperature profile of the simulation, it is not surprising to see on one hand the underestimation of the mechanical thickness and on the other hand a systematic overestimation of partial melting by the spherical annulus compared to the 3D. The main reason explaining these differences is that the spherical annulus will consistently overestimate the overall mantle temperature, leading to a hotter temperature profile, thus directly affecting the degree of melting and the thickness of the mechanical lithosphere.

In the case of a Mars-like structure (Figure 8b, e) the differences between 2D and 3D are larger, in particular in the case of partial melting, which the annulus will overestimate by a maximum of 30% at around 1.5 Gyr. The mechanical thickness will be underestimated on average by 10 %. In particular the differences in partial melting could lead to an overestimation of the crustal thickness in the 2D spherical annulus geometry. This in turn could lead to more crustal production due to a mechanism called "crustal blanketing" (e.g., Schumacher & Breuer, 2006), in which the reduced thermal conductivity of the crust will prevent efficient cooling of the mantle. A higher crustal production rate could then lead to a stronger depletion of the mantle in crustal components and volatile elements. Hence, care should be taken when the spherical annulus geometry is employed to study partial melting and subsequent crust production or degassing in particular for planets with an intermediate radius ratio, like Mars or Venus. These processes and the differences between 2D and 3D geometries for such scenarios need to be quantified in future studies.

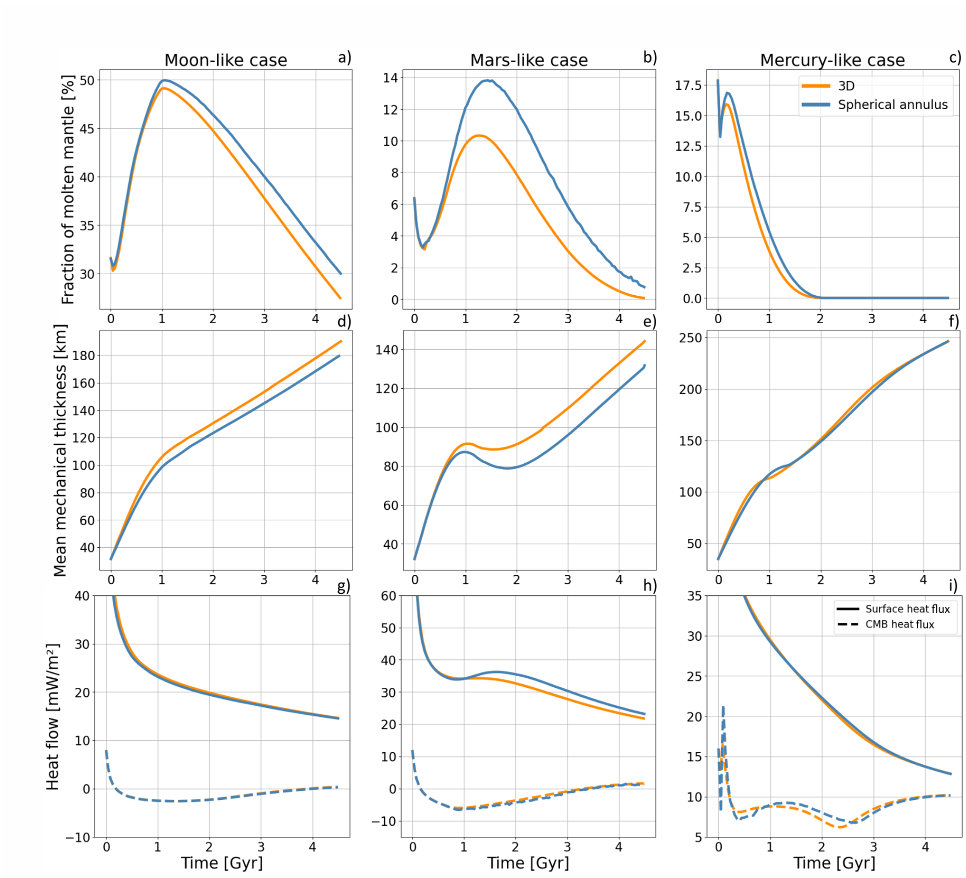

Figure 8: Timeseries of the three scenario investigated (from left to right; the Moon, Mars and Mercury). First row shows the fraction of molten mantle (in %) at a given time in the evolution for each planet, second row shows the mechanical thickness of the lithosphere (in km) during the evolution, and the third row shows the CMB and surface heat fluxes (in $\mathrm{mW\,m^{-2}}$). Since the cylindrical geometry shows the largest difference to the 3D, it was not included in this comparison. All the equations used in order to compute these quantities are described in the SI.

5 Conclusions

The main goal of this study is to provide a systematic comparison between different geometries in order to determine how accurate can 2D geometries reproduce 3D results. To this end, we investigated (scaled and non-scaled) 2D cylinder, 2D spherical annulus, and 3D spherical shell geometries in a series of scenarios. We started with isoviscous steady-state models, included the effects of a temperature dependent viscosity, and finally tested the different geometries for thermal evolution setups. Our main findings are the following:

1. While it is obvious that a 3D geometry should be preferred over a 2D one, due to the high computational cost, this may not always be feasible. Applying models with different complexities, we demonstrated that the 2D spherical annulus geometry is able to reproduce the 3D models much better than the 2D cylinder, in particular for the low radius ratio setups. The latter is also clearly seen when modeling the thermal evolution of the Moon.

2. For steady-state scenarios, our models show that the 2D geometries will mostly overestimate the mean temperature compared to 3D, a result largely explained by the geometry of mantle plumes (i.e., sheet-like in 2D vs. columnar-like in 3D). This discrepancy decreases with an increasing Rayleigh number but is more accentuated for low-radius ratio cases, a result already observed by Guerrero et al. (2018). The differences in temperature between the 2D and 3D geometries decreases for mixed heated cases (i.e., heated both from below and from within). This is especially true in the case of the spherical annulus, since the spherical annulus is a geometry which uses the same cell volumes as a 3D spherical shell.
3. We find that for intermediate ratios of the inner to outer radius (e.g., Mars-like thermal evolution case), the differences in the results for the 2D and 3D geometries are larger than for extreme radius ratios. In contrast to the temperature-dependent steady-state cases, where the difference in surface heat flux and stagnant lid thickness between 2D geometries and 3D geometries is largest for high radius ratios, the difference obtained for Mercury-like evolution parameters is minimal. This is due to the low Rayleigh number of Mercury that leads to the transition to a conductive state during its thermal history.
4. Care needs to be taken when studying melting processes with the spherical annulus in thermal evolution setups with intermediate radius ratios (e.g., Mars and Venus), as this geometry might overestimate crustal production by up to 30% compared to a 3D simulation leading to a different thermal history of the interior.

Future studies need to test the accuracy of the 2D spherical annulus in reproducing the 3D spherical shell geometry in more complex scenarios considering variable thermal conductivity and expansivity (Tosi, Yuen, et al., 2013), chemical buoyancy (Nakagawa et al., 2010), as well as partial melting of the mantle and its influence on thermal evolution.

Data Availability Statement

Supplementary datasets containing all values shown in tables and figures are available upon request on Zenodo : https://doi.org/10.5281/zenodo.8047757

Acknowledgments

Authors of this study gratefully acknowledge the financial support and endorsement from the DLR Management Board Young Research Group Leader Program and the Executive Board Member for Space Research and Technology. The authors also acknowledge the computational resources provided by the CARA cluster of the German Aerospace Center. Part of this work was performed on the HoreKa supercomputer funded by the Ministry of Science, Research and the Arts Baden-Württemberg and by the Federal Ministry of Education and Research.

References

Breuer, D., & Moore, W. B. (2015). Dynamics and Thermal History of the Terrestrial Planets, the Moon, and Io. *Treatise on Geophysics*, *10*(Second Ed.), 299–348. doi: 10.1016/B978-0-444-53802-4.00173-1

Deschamps, F., Tackley, P. J., & Nakagawa, T. (2010, July). Temperature and heat flux scalings for isoviscous thermal convection in spherical geometry. *Geophysical Journal International*, *182*(1), 137-154. doi: 10.1111/j.1365-246X.2010.04637.x

Frank-Kamenetskii, D. (1969). *Diffusion and Heat Transfer in Chemical Kinetics.*

Grott, M., & Breuer, D. (2008, 01). The evolution of the martian elastic lithosphere and implications for crustal and mantle rheology. *Icarus: International Journal of Solar System Studies*, *193*, 503-515.

Guerrero, J. M., Lowman, J. P., Deschamps, F., & Tackley, P. J. (2018). The influence of curvature on convection in a temperature-dependent viscosity fluid: Implications for the 2-d and 3-d modeling of moons. *Journal of Geophysical Research: Planets*, *123*(7), 1863-1880. Retrieved from `https://agupubs.onlinelibrary.wiley.com/doi/abs/10.1029/2017JE005497` doi: https://doi.org/10.1029/2017JE005497

Hernlund, J. W., & Tackley, P. J. (2008). Modeling mantle convection in the spherical annulus. *Physics of the Earth and Planetary Interios*, *171*, 48-54. doi: 10.1016/j.pepi.2008.07.037

Hirth, G., & Kohlstedt, D. (2003, January). Rheology of the upper mantle and the mantle wedge: A view from the experimentalists. *Washington DC American Geophysical Union Geophysical Monograph Series*, *138*, 83-105. doi: 10.1029/138GM06

Hüttig, C., & Stemmer, K. (2008a). Finite volume discretization for dynamic viscosities on Voronoi grids. *Physics of the Earth and Planetary Interios*, *171*(1–4), 137–146. doi: 10.1016/j.pepi.2008.07.007

Hüttig, C., & Stemmer, K. (2008b). The spiral grid: A new approach to discretize the sphere and its application to mantle convection. *Geochem. Geophys. Geosyst.*, *9*, Q02018. doi: 10.1029/2007GC001581

Hüttig, C., Tosi, N., & Moore, W. B. (2013). An improved formulation of the incompressible Navier-Stokes equations with variable viscosity. *Physics of the Earth and Planetary Interios*, *40*, 113–129.

Jarvis, G. T. (1993, March). Effects of curvature on two-dimensional models of mantle convection: Cylindrical polar coordinates. *JGR: Solid Earth*, *98*(B3), 4477-4485. doi: 10.1029/92JB02117

Jarvis, G. T., Glatzmaierand, G. A., & Vangelov, V. I. (1995, January). Effects of curvature, aspect ratio and plan form in two- and three-dimensional spherical

models of thermal convection. *Geophysical and Astrophysical Fluid Dynamics*, *79*(1), 147-171. doi: 10.1080/03091929508228995
Kageyama, A., & Sato, T. (2004, 03). "yin-yang grid": An overset grid in spherical geometry. *Geochemistry Geophysics Geosystems*, *5*. doi: 10.1029/2004GC000734
Kameyama, M. (2022, 07). Numerical experiments on thermal convection of highly compressible fluids with variable viscosity and thermal conductivity in 2-D cylindrical geometry: implications for mantle convection of super-Earths. *Geophysical Journal International*, *231*(2), 1457-1469. Retrieved from `https://doi.org/10.1093/gji/ggac259` doi: 10.1093/gji/ggac259
Karato, S. I., & Wu, P. (1993). Rheology of the upper mantle: a synthesis. *Science*, *260*, 771–778.
Mulyukova, E., Steinberger, B., Dabrowski, M., & Sobolev, S. V. (2015). Survival of llsvps for billions of years in a vigorously convecting mantle: Replenishment and destruction of chemical anomaly. *Journal of Geophysical Research: Solid Earth*, *120*(5), 3824-3847. Retrieved from `https://agupubs.onlinelibrary.wiley.com/doi/abs/10.1002/2014JB011688` doi: https://doi.org/10.1002/2014JB011688
Nakagawa, T., & Tackley, P. J. (2004). Effects of a perovskite-post perovskite phase change near core-mantle boundary in compressible mantle convection. *Geophys. Res. Lett.*, *31*(L16611). doi: 10.1029/2004GL020648
Nakagawa, T., Tackley, P. J., Deschamps, F., & Connolly, J. A. D. (2010). The influence of MORB and harzburgite composition on thermo-chemical mantle convection in a 3-D spherical shell with self-consistently calculated mineral physics. *Earth Planet. Sci. Lett.*, *296*, 403–412. doi: 10.1016/j.epsl.2010.05.026
Noack, L., & Tosi, N. (2012). *High-performance modelling in geodynamics.* Integrated Information and Computing Systems for Natural, Spatial and Social Sciences.
Padovan, S., Tosi, N., Plesa, A.-C., & Ruedas, T. (2017). Impact-induced changes in source depth and volume of magmatism on Mercury and their observational signatures. *Nature communications*, *8*(1), 1945. doi: 10.1038/s41467-017-01692-0
Roberts, J. H., & Zhong, S. (2006). Degree-1 convection in the Martian mantle and the origin of the hemispheric dichotomy. *J. Geophys. Res. (Planets)*, *111*.
Schubert, G., Turcotte, D. L., & Olson, P. (2001). *Mantle convection in the Earth and planets.* Cambridge: Cambridge University Press.
Schumacher, S., & Breuer, D. (2006). Influence of a variable thermal conductivity on the thermochemical evolution of Mars. *J. Geophys. Res.*, *111*(E02006). doi: 10.1029/2007GL030083
Stegman, D. R., Jellinek, A. M., Zatman, S. A., Baumgardner, J. R., & Richards, M. A. (2003). An early lunar core dynamo driven by thermochemical mantle convection. *Nature*, *421*, 143–146.
Stevenson, D. J., Spohn, T., & Schubert, G. (1983). Magnetism and Thermal Evolution of the Terrestrial Planets. *Icarus*, *54*, 466–489.
Taylor, G. J. (2013). The bulk composition of mars. *Geochemistry*, *73*(4), 401–420.
Taylor, S. R. (1982, September). Lunar and terrestrial crusts: a constrast in origin and evolution. *Physics of the Earth and Planetary Interiors*, *29*(3-4), 233-241. doi: 10.1016/0031-9201(82)90014-0
Tosi, N., Grott, M., Plesa, A.-C., & Breuer, D. (2013). Thermo-chemical evolution of Mercury's interior. *J. Geophys. Res. (Planets)*. (accepted) doi: 10.1002/jgre.20168
Tosi, N., Yuen, D. A., de Koker, N., & Wentzcovitch, R. M. (2013). Mantle dynamics with pressure- and temperature-dependent thermal expansivity and conductivity. *Physics of the Earth and Planetary Interios*, *217*, 48–58. doi:

10.1016/j.pepi.2013.02.004

van Keken, P. E. (2001). Cylindrical scaling for dynamical cooling models of the earth. *Physics of the Earth and Planetary Interios*, *124*, 119–130.

van Keken, P. E., & Yuen, D. A. (1995). Dynamical influences of high viscosity in the lower mantle induced by the steep melting curve of perovskite: Effects of curvature and time dependence. *Journal of Geophysical Research: Solid Earth*, *100*(B8), 15233-15248. Retrieved from https://agupubs.onlinelibrary.wiley.com/doi/abs/10.1029/95JB00923 doi: https://doi.org/10.1029/95JB00923

van Zelst, I., Crameri, F., Pusok, A. E., Glerum, A., Dannberg, J., & Thieulot, C. (2022). 101 geodynamic modelling: how to design, interpret, and communicate numerical studies of the solid Earth. *Solid Earth*, *13*(3), 583–637. Retrieved from https://se.copernicus.org/articles/13/583/2022/ doi: 10.5194/se-13-583-2022

Yu, S., Tosi, N., Schwinger, S., Maurice, M., Breuer, D., & Xiao, L. (2019). Overturn of ilmenite-bearing cumulates in a rheologically weak lunar mantle. *Journal of Geophysical Research: Planets*, *124*(2), 418-436. Retrieved from https://agupubs.onlinelibrary.wiley.com/doi/abs/10.1029/2018JE005739 doi: https://doi.org/10.1029/2018JE005739

Approximating 3D Models of Planetary Evolution in 2D: A Comparison of Different Geometries

A. Fleury[1], A.-C. Plesa[1], C. Hüttig[1], D. Breuer[1]

[1]Institute of Planetary Research, German Aerospace Center (DLR), Berlin, Germany

Key Points:

- Interior dynamics models using the 2D spherical annulus geometry match the results of a 3D spherical shell better than the 2D cylinder.
- The difference between 2D and 3D geometries decreases when models are heated from below by the core and from within by radioactive elements.
- The spherical annulus shows negligible differences to 3D for the thermal evolution of Mercury and the Moon, and acceptable values for Mars.

Corresponding author: Aymeric Fleury, `aymeric.fleury@dlr.de`

Abstract

Regardless of the steady increase of computing power during the last decades, 3D numerical models continue to be used in specific setups to investigate the thermochemical convection of planetary interiors, while the use of 2D geometries is still favored in most exploratory studies involving a broad range of parameters. The 2D cylindrical and the more recent 2D spherical annulus geometries are predominantly used in this context, but the extent to how well they reproduce the 3D spherical shell in comparison to each other, and in which setup, has not yet been extensively studied. Here we performed a thorough and systematic study in order to assess which 2D geometry reproduces best the 3D one. In a first set of models, we investigated the effects of the geometry on thermal convection in steady-state setups while varying a broad range of parameters. Additional thermal evolution models of three terrestrial bodies, respectively Mercury, the Moon, and Mars, which have different interior structures, were used to compare the 2D and 3D geometries. Our study shows that the spherical annulus geometry improves results compared to cylindrical geometry when reproducing 3D models. Our results can be used to determine for which setup acceptable differences are expected when using a 2D instead of a 3D geometry.

Plain Language Summary

In geodynamic modeling, numerical models are used in order to investigate how the interior of a terrestrial planet evolves from the earliest stage, after the planetary formation, up to present day. The mathematical equations that are used to model the physical processes in the interior of rocky planets are discretized and solved using geometric meshes. The most commonly used geometries are the 3D spherical shell, the 2D cylinder, and the 2D spherical annulus. While being the most accurate and realistic, the 3D geometry is expensive in terms of computing power and time of execution. On the other hand, 2D geometries provide a reduced accuracy but are computationally faster. Here we perform an extensive comparison between 2D and 3D geometries in scenarios of increasing complexity. The 2D spherical annulus geometry shows much closer results to the 3D spherical shell when compared to the 2D cylinder and should be considered in 2D modeling studies.

1 Introduction

Geodynamic modeling is a powerful approach to investigate the dynamics of the mantle and lithosphere of terrestrial planets and to explore the evolution of their interior that is not directly observable. Such models vary in their complexity and often employ different geometries to investigate physical processes such as mantle melting and cooling, and the generation of a magnetic field. When using these models to interpret specific observations of the Earth and other planets, care must be taken in particular for the choice of geometry (see Noack & Tosi, 2012, for an overview of geometries), as this may significantly impact quantities such as the mantle temperature, the convection velocity, and the heat flux of the simulations.

The role of two-dimensional geometry studies in the field of thermochemical mantle convection modeling is still predominant despite an ever-increasing computing power. Although the formulation of 3D grids has seen improvements in previous years with the Yin-Yang grid (Kageyama & Sato, 2004) and the spiral grid (Hüttig & Stemmer, 2008a) among others; simulations with a full spherical shell geometry remain highly expensive in terms of computational power, hence making them inappropriate to study broad ranges of parameters or conduct large exploratory studies. As an alternative, geometrical analogues to the 3D spherical shell have been extensively used, namely the 2D spherical axisymmetric (van Keken & Yuen, 1995) and the more popular cylindrical geometry (Jarvis, 1993). The 2D axi-symmetric geometry has been used in earlier studies of mantle convection (e.g., van Keken & Yuen, 1995; Jarvis et al., 1995), but in addition to the artificial boundaries formed by the poles which trap down- and up-wellings, an asymmetry between the polar and the equatorial regions exists (van Keken, 2001). The cylindrical geometry on the other hand, while resolving the problems of the artificial boundaries at the poles imposed by the axi-symmetric geometry, still exhibits an important drawback. The ratio of the two surfaces (the planetary surface and the core surface) is different in the cylindrical geometry compared to the spherical shell. This leads to a mismatch in heat flux values between these geometries, as the heat flux of the core mantle boundary (CMB) is underestimated and the surface heat flux is overestimated when comparing to a spherical shell with the same ratio between the core and planet radius (i.e., radius ratio).

In order to mitigate this problem, van Keken (2001) introduced a re-scaling of the 2D cylindrical geometry such that the ratio of outer and inner areas of the cylinder matches the ratio obtained for the spherical shell. This scaling, however, while correcting the surface ratio discrepancy of the cylinder, still uses the volume of a cylinder. Additionally, this re-scaling creates an artificially smaller core, which in turn modifies the convection pattern in the mantle, leading for example to a crowding of the plumes near the CMB, a behavior that would not be observed in a 3D spherical shell, when using the original, non-scaled radii.

To overcome this major drawback of the cylindrical geometry, another 2D geometry called "spherical annulus" has been proposed by Hernlund and Tackley (2008). This geometry effectively uses a second degree of curvature and considers the same surfaces and volumes as the 3D geometry. Since no re-scaling is necessary for this geometry, it keeps the same radius ratio as the 3D one. In the study of Hernlund and Tackley (2008), the spherical annulus showed promising results to approximate the 3D spherical geometry with mean temperature and Nusselt number well reproduced for steady-state thermal convection calculations. While these results a highly valuable, there are only for the case of an Earth-like radius ratio and only consider thermal convection simulations in the Boussinesq approximation.

More recently, Guerrero et al. (2018) performed a more extensive study with the spherical annulus for stagnant lid convection models and compared the temperature distribution between the spherical annulus and the spherical shell. However, an extensive study investigating the ability of the 2D spherical annulus to reproduce results obtained in a 3D spherical shell and a systematic comparison with the 2D cylinder for various setups has never been conducted so far.

In this study, we present simulations of thermal convection in the 2D spherical annulus and compare the results to the 2D cylinder and the 3D spherical shell. In a first part we focus on simple steady-state convection models using the Boussinesq approximation. We vary the Rayleigh number, the radius ratio, and the heating mode for isoviscous cases and run additional temperature-dependent viscosity models to determine which of the two 2D geometries (i.e., cylinder or spherical annulus) is able to best reproduce the 3D results. The set of equations that were used for this comparison are described in Section 2.1, the grid geometries are displayed in Section 2.2, and a description of the cases investigated here is available in Section 2.3. A detailed analysis of the results is presented in Section 2.4.

In a second step, we run more complex simulations of thermal evolution with the same geometries in three separate scenarios. We use Moon-like, Mars-like, and Mercury-like thermal evolution models to investigate how well the 2D spherical annulus reproduces the results of the 3D spherical shell geometry. The three planetary bodies were chosen since they cover a wide range of interior structures and they are all thought to have been in a stagnant lid regime over their entire thermal history, which makes them comparable in terms of their tectonic regime (Breuer & Moore, 2015). In Section 3.1 we list the equations used for the thermal evolution models. A description of the employed parameters and setup of the models is given in Section 3.2. The results are described in Section 3.3. A discussion of the steady-state and thermal evolution models is presented in Section 4, followed by conclusions in Section 5.

2 Steady-state mantle convection

In a first set of calculations we focus on the comparison between steady-state calculations in 2D and 3D geometries. For this purpose we test a large number of parameter combinations for isoviscous models and temperature-dependent viscosity.

2.1 Mathematical model

Fully dynamical models of mantle convection allow us to investigate the spatial and temporal evolution of mantle flow. These models solve the conservation equations of mass, momentum, and energy. Here, the conservation equations are scaled using the mantle thickness D as length scale, the temperature drop across the mantle ΔT as temperature scale and the thermal diffusivity κ as time scale. A Table listing the scaling factors is available in the Supplementary Information, SI (Table S1). By assuming a Newtonian rheology, an infinite Prandtl number, and considering the Boussinesq approximation (Schubert et al., 2001; van Zelst et al., 2022), the non-dimensional conservation equations read:

$$\begin{aligned} \nabla \cdot \mathbf{u} &= 0, && (1) \\ \nabla \cdot \left(\eta \left(\nabla \mathbf{u} + (\nabla \mathbf{u})^T\right)\right) + RaT\mathbf{e}_r - \nabla P &= 0, && (2) \\ \frac{DT}{Dt} - \nabla^2 T - H &= 0. && (3) \end{aligned}$$

In Equations 1 – 3, $\mathbf{u}$ is the velocity vector, η is the viscosity, T is the temperature, $\mathbf{e}_r$ is the radial unit vector, P is the dynamic pressure, and t is the time.

The parameter Ra denotes the thermal Rayleigh number, a non-dimensional number, which controls the vigor of the convection in the mantle. H is the internal heating rate of the mantle that is given by $\frac{Ra_Q}{Ra}$, where Ra_Q denotes the Rayleigh number associated with internal heating. The Rayleigh numbers Ra and Ra_Q read:

$$Ra = \frac{\rho_{ref} g_{ref} \alpha_{ref} \Delta T D^3}{\kappa_{ref} \eta_{ref}}, \quad RaQ = \frac{\rho_{ref}^2 g_{ref} \alpha_{ref} H D^5}{\kappa_{ref} \eta_{ref} k_{ref}}, \tag{4}$$

where ρ_{ref} is the reference density, g_{ref} is the reference gravitational acceleration, α_{ref} is the reference thermal expansivity, κ_{ref} is the reference thermal diffusivity, η_{ref} is the reference viscosity, k_{ref} is the reference thermal conductivity, and H is the internal heating rate in W/kg.

For the steady-state models, we use a constant or temperature-dependent viscosity that follows the Frank-Kamenetskii approximation (Frank-Kamenetskii, 1969), which is a linearized form of the Arrhenius law:

$$\eta(T) = \exp(\Delta\eta_T (T_{ref} - T)), \tag{5}$$

The parameter $\Delta\eta_T$ is the viscosity contrast due to temperature and T_{ref} is the reference temperature at which a non-dimensional viscosity equal to 1 is attained. For the thermal evolution simulations presented further in this study, we use another parametrization of the viscosity (Eq. 9), which is discussed more in-depth in the Section 3.1.

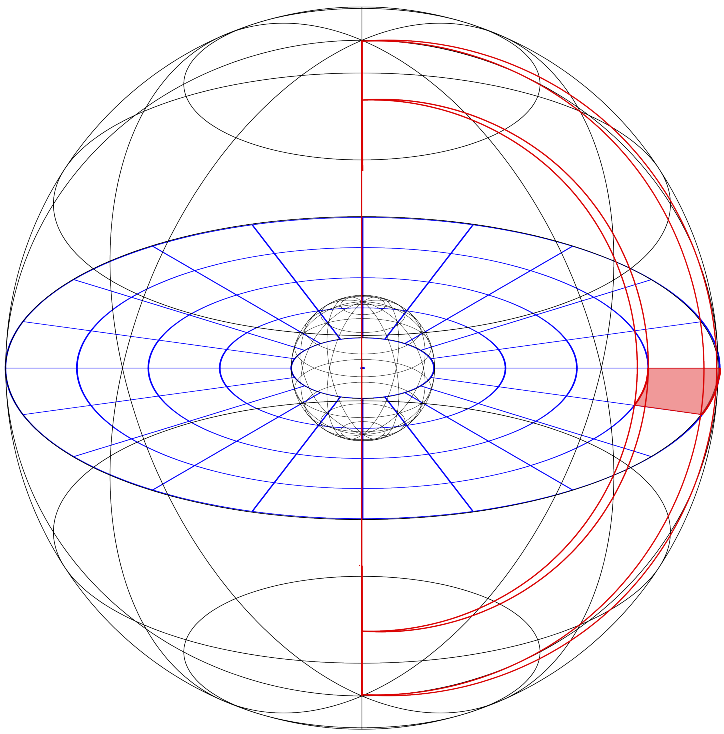

Figure 1: Representation of a cell of the spherical annulus geometry, in red, its effective volume. The cylindrical geometry is represented in blue, on the equatorial plane. The red area represented corresponds to the intersection of the spherical annulus cell with the equatorial plane. When looking at the grid from a polar point of view, its visualization becomes thus indistinguishable from the cylindrical cell.

2.2 Grid geometries

We use the numerical code Gaia (Hüttig & Stemmer, 2008a, 2008b; Hüttig et al., 2013) to model the mantle convection in the interior of rocky planets. Gaia solves the conservation equations (Eq. 1 – 3) in their dimensionless form in 2D and 3D geometries. For the 2D geometry, we use both the classical cylindrical geometry (van Keken, 2001) and the spherical annulus geometry following the approach of Hernlund and Tackley (2008). In the 2D cylindrical geometry, the areas and volumes of the grid cells are typically formulated using the equations for a cylinder; however, what makes the particularity of the spherical annulus geometry, is the addition of a virtual thickness to the cylindrical geometry which varies with the radius r. Thus the spherical annulus has a second degree of curvature, and uses an effective 3-dimensional formulation for the areas and volumes, as represented on Figure 1 (a more detailed description of the spherical annulus geometry is available in Section S3 of the SI).

The 2D cylindrical geometry is scaled according to the scaling introduced by van Keken (2001), where the inner and outer radii of the cylinder grid (i.e., the core radius and the planetary radius, respectively) are changed such that the ratio between the outer and inner areas of the cylinder matches the ratio obtained in a 3D spherical shell geometry. The equations used to correct the inner and outer radii of the cylinder are the following:

$$\frac{r_{oc}}{r_{ic}} = \frac{r_{os}^2}{r_{is}^2}, \qquad\qquad r_{oc} - r_{ic} = r_{os} - r_{is}, \tag{6}$$

where r_{ic} and r_{oc} are the inner and the outer radius of the cylinder, respectively. The inner and outer radii of the spherical shell are denoted by r_{is} and r_{os}, respectively. In the following, we will refer to this type of geometry that considers the rescaling of the inner and outer radii as the "scaled cylinder geometry".

2.3 Case definition

In the first part of this study, we performed steady-state simulations in order to investigate the effects of the ratio of the inner to outer radius and of heating modes on the results obtained with the 2D cylindrical, 2D spherical annulus, and 3D spherical shell geometry. Our aim is to compare 2D and 3D geometries and determine for which scenarios does the 2D spherical annulus give closer results to the 3D compared to the 2D cylinder. To this end, we use models heated from below (purely bottom-heated), from within (purely internally-heated), and from both below and within (mixed heated). We use an initial random perturbation of the temperature field with an amplitude of 5%, vary the Rayleigh number Ra of our simulations from 10^4 up to 10^8, and the radius ratio f from 0.2 to 0.8 for our isoviscous setup.

For the 2D geometries, we use between 1.1×10^4 and 6.7×10^4 grid points for low Rayleigh number simulations and between 4.8×10^4 and 4.1×10^5 for simulations with a Rayleigh number higher than 10^6. For the 3D geometries, we use between 2.04×10^6 and 2.94×10^6 grid points. A more in depth description of each grid and its associated lateral and radial resolution is available in the SI. A short comparison of our results to the ones of Hernlund and Tackley (2008) for isoviscous steady-state cases is presented in Section S4 of the SI.

Each mesh has a prescribed temperature and free-slip velocity as boundary conditions. The temperature of the upper boundary T_{surf} is set to zero, while the one of the lower boundary is set to one for the bottom heated and mixed heated cases. For the purely internally heated cases we use a zero heat flux at the core-mantle boundary.

The simulations are ran until a statistical steady-state is reached. Then, output quantities such as the average temperature, root-mean-square velocity, and top temperature gradient are computed using an average over the last 10% of the simulation. While for purely steady-state models this is the same as taking the last output, for quasi steady-state time-dependent or periodic models this ensures to retrieve representative average values. The top temperature gradient here is the temperature gradient at the top of the domain, calculated between the last two shells of the grid.

An additional, more complex set of simulations includes the effect of the temperature dependence of the viscosity, and leads to the formation of a stagnant lid at the top of the convecting domain. These simulation represent simplified Moon-like ($f = 0.2$), Mars-like ($f = 0.5$), and Mercury-like ($f = 0.8$) scenarios. We use here thermal and radiogenic Ra numbers with values similar to those expected for planetary mantles, i.e., $Ra = 5 \times 10^6$ and $Ra_Q = 5 \times 10^7$ (see values of Ra and Ra_Q in Table 1). We use the Frank Kamenetskii parametrization for the viscosity (Eq. 5) and set a viscosity contrast $\Delta\eta_T$ to 10^8 at a reference temperature T_{ref} of 0.5 to ensure that we are in a stagnant lid convection regime. In this setup, the total number of nodes used for the 2D grids lies between 4.8×10^4 and 2.8×10^5; while for the 3D simulations, the total number of nodes is 2.9×10^6.

In total, we run 180 isoviscous simulations and 36 temperature-dependent viscosity cases. All parameters and the grid resolutions for these steady-state simulations are listed in Table S2 in the SI.

2.4 Results

2.4.1 Isoviscous convection

For the first set, consisting of isoviscous simulations, we provide a thorough and systematic comparison between the 3D spherical grid and the two 2D geometries, namely the spherical annulus and the cylindrical geometry. A summary of the comparison is shown in Figure 2.

Here, the analysis of the 180 simulations has been summarized into three subplots one for each heating mode. Each subplot contains two rows showing for each the annulus geometry (first row) and the scaled cylindrical geometry (second row), respectively, the relative error to the 3D results. The computation details of the relative error can be found in the SI (Section S5) along with tables containing the values for each simulation in CSV format. Figure 2 shows that the mean domain temperature of the 3D geometry is more accurately reproduced by the spherical annulus geometry than by the cylindrical one in every heating mode, up to values of $Ra = 10^7$. This difference is even more noticeable in the low radius ratiosetups (i.e., $f = 0.2$ and 0.4), which can be seen for the purely bottom heated and mixed heated scenarios. We also see for the purely internal heated cases and high Rayleigh number cases (i.e., $Ra = 10^7$ and $Ra = 10^8$) that this difference is even more dramatic with an overestimation of the temperature in the cylindrical geometry by up to $\sim 20\%$ for the small a radius ratio (i.e., $f = 2$) and reduces to only a few percent in the spherical annulus.

In the case of the root mean square velocity, we see a general increase of the accuracy with the spherical annulus geometry, however this increase is less pronounced than what is observed for the mean temperature. We see a slightly better match for the purely bottom heated and mixed heated setups, where simulations with $Ra < 10^7$ go from being slightly underestimated by the cylinder to slightly overestimated by the annulus. However, the cases with $Ra \geq 10^7$ show a net improvement, with an underestimation decreasing for all the cases with a radius ratio higher than 0.2. For the setup with a purely internal heating, however, almost no improvement is visible, with the notable exception of the simulation with a $Ra = 10^8$ and a radius ratio of 0.2 being overestimated by $\sim$ 40% in the case of the cylinder, which turns to be overestimated only by $\sim 20\%$ in the case of the spherical annulus.

In comparison to the cylinder, the spherical annulus, gives less conclusive results for the top temperature gradient. We can see an improvement in case of small radius ratios (i.e., $f = 0.2$) with either purely internal heating or mixed heating, or in the case of high Rayleigh numbers (i.e., $Ra \geq 10^7$) for purely internal heated cases. Otherwise, for the majority of the setups and heating modes, the spherical annulus does not show significant improvement in reproducing the 3D values compared to the scaled cylindrical geometry. A comparison of the temperature gradient at the top of the mantle shows that the spherical annulus is hardly able to reproduce the 3D values more accurately than the scaled cylindrical geometry, with the notable exception of low radius ratios of around $f = 0.2$.

2.4.2 Stagnant lid convection

In the second part of the steady-state simulations, we modeled stagnant lid convection while varying the heating mode, the radius ratio, and the geometry in order to study the accuracy of the spherical annulus geometry (see SI, Table S2). In this type of setup, where the viscosity is strongly dependent on temperature, the convection is expected to operate in a stagnant lid regime. This rigid layer that forms at the top of the domain restricts convective heat transfer to the deep interior.

The results are summarized in Figure 3, where we report the relative error of the 2D cylindrical, 2D scaled cylindrical, and 2D spherical annulus geometry to the 3D spherical shell. Here we inspect the mean temperature, the root mean square velocity, the top

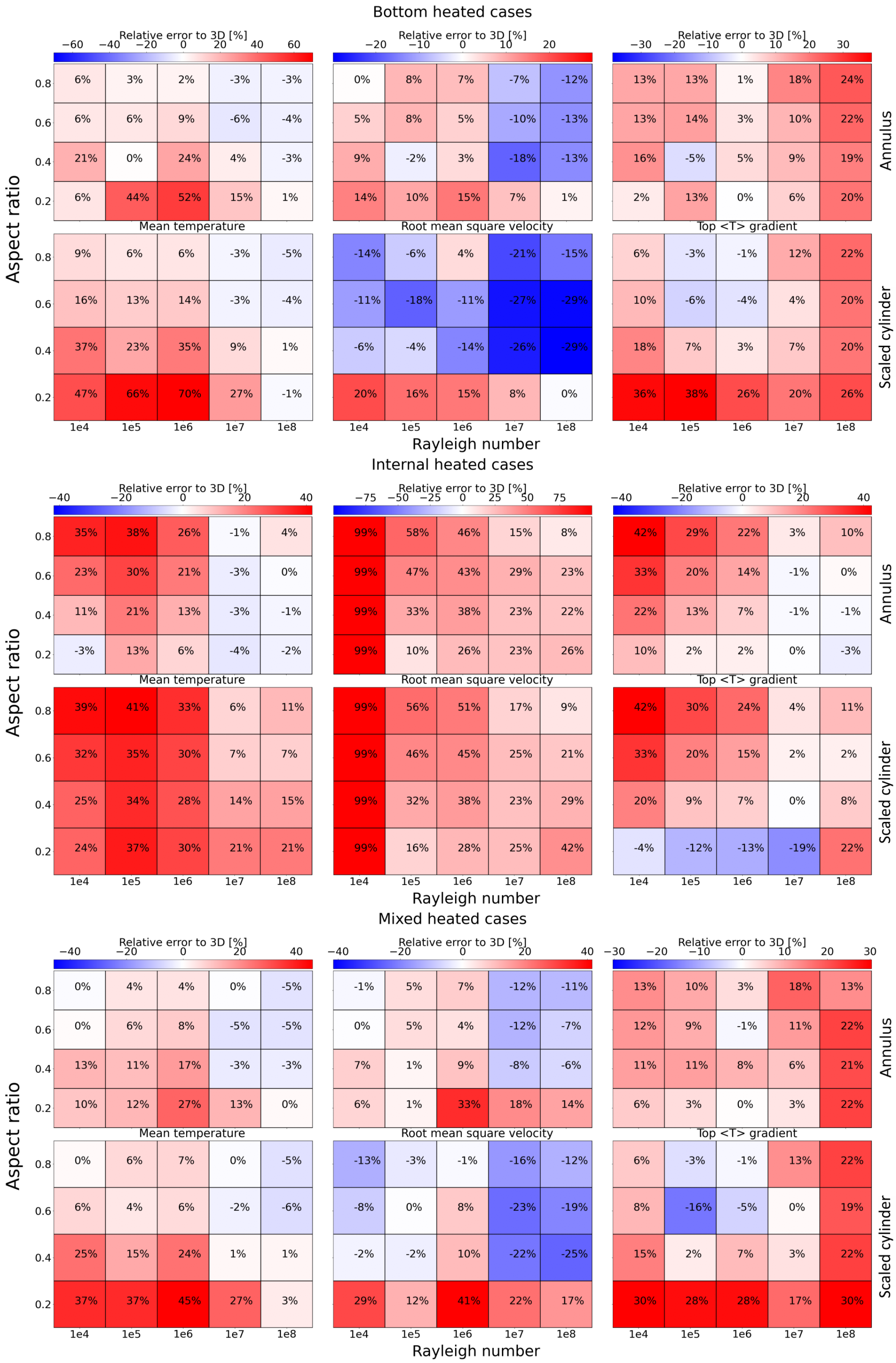

Figure 2: Averaged computed relative error to the 3D geometry with 3 different heating modes, i.e., purely basal heated (top row), purely internal heated (middle row), or mixed heated (bottom row) for steady-state isoviscous convection simulations. For each heating mode the first line of plots shows the relative errors for the spherical annulus and the second line represents the scaled cylinder. The thermal Rayleigh number and internal Rayleigh number vary from 10^4 to 10^8 and the radius ratio from 0.2 to 0.8. The radius ratio indicated on the plot is the one corresponding to the reference 3D simulations. In the case of the cylinder, the radius ratio is scaled, thus a 0.2 radius ratio becomes 0.04 following the scaling formula from van Keken (2001) (eq. 6). For columns from left to right, relative error of the mean temperature, of the v_{rms}, and of the top temperature gradient are shown.

temperature gradient, and the stagnant lid thickness. For each simulation we use a Ra of 10×10^6 and Ra_Q of 10×10^7.

In Figure 3, when considering purely basal heating, we see that the spherical annulus is overall better at reproducing the 3D values compared to the scaled and non-scaled cylinder. The highest discrepancy is observed for the radius ratio $f = 0.2$, with $> 50\%$ of overestimation on average for the 2D geometries. For the spherical annulus, the mean temperature matches best the one of the 3D spherical shell when the radius ratio increases, an effect also seen for the $\mathrm{v_{rms}}$. The top temperature gradient does not follow this pattern, however, while the stagnant lid error is the lowest for $f = 0.5$. The highest difference to the 3D for the low radius ratio setups ($f = 0.2$) in the purely bottom heated setup that we found in our models is in agreement with Guerrero et al. (2018). The study by Guerrero et al. (2018) considered stagnant lid convection with only basal heating, and observed that for small radius ratio setups, the spherical annulus would systematically show a hotter temperature when compared to the 3D. This behavior is indeed confirmed by our simulations, where we can observe that the different geometry of plumes between the spherical annulus and the spherical shell create considerable differences in temperature in the low radius ratio and bottom heated simulations. Plumes in a 2D geometry are rather sheet-like than column-like as they are in a 3D geometry. This leads to a warmer temperature in the 2D geometries compared to the 3D as being the consequence of a topological difference between flows in a spherical shell and spherical annulus, as explained by Guerrero et al. (2018). Moreover, this difference is strongly accentuated for low radius ratios, where the number of plumes is small and such geometrical effects significantly affect the results. For a better illustration of this behavior we refer the reader to Figure S5 of the SI. The increase of temperature differences with increasing f was also observed by Guerrero et al. (2018) and is confirmed by our results.

In the case of a purely internally heated case, we see that the annulus fares remarkably better than the cylindrical geometries and that the average relative error of the mean temperature, the $\mathrm{v_{rms}}$, and top temperature gradient diminish as the radius ratio decreases. The highest radius ratio (i.e., $f = 0.8$) shows here the highest discrepancy between 2D and 3D, with more than 50% and 20% of overestimation for the v_{rms} and the top temperature gradient respectively, while the stagnant lid is underestimated on average by 15%. When taking a closer look at the simulations, it appears that, the internal heating simulations in 2D have a tendency to require more convective strength in order to transport the same amount of heat in the domain compared to a 3D simulation, as already shown in Hernlund and Tackley (2008). This peculiarity when investigating the temperature and velocity distribution will apparently create a larger amount of downwellings in the case of a 3D model for a given internal heating rate when compared to a 2D one. This can be seen on the Figure S7 of the SI.

For cases heated both from below and from within (i.e., mixed heated cases), the spherical annulus is showing the best results for the mean temperature, the top temperature gradient, and the stagnant lid thickness when the radius ratio is the lowest (i.e., $f = 0.2$). For the highest radius ratio considered here (i.e., $f = 0.8$), the results obtained with the spherical annulus and the cylinder geometries show similar errors, with the exception of v_{rms} that seems to be best reproduced by the scaled cylinder geometry.

When combining purely basal heating with internal heating, the main discrepancy previously arising from the low radius ratio and purely basal heated simulations seems to be mitigated by the addition of internal heating. The difference in the temperature distribution between the spherical annulus and the spherical shell tends to disappear (see Figure S7 of the SI).

In summary, for the stagnant lid cases presented here, the mean temperature is overall better reproduced by the spherical annulus independently of the radius ratio or heating mode. Additionally, in the intermediate to low radius ratio simulations ($f \leq 0.5$), the spherical annulus can also reproduce the 3D velocities, the top temperature gradient, and the stagnant lid better than the cylinder geometry.

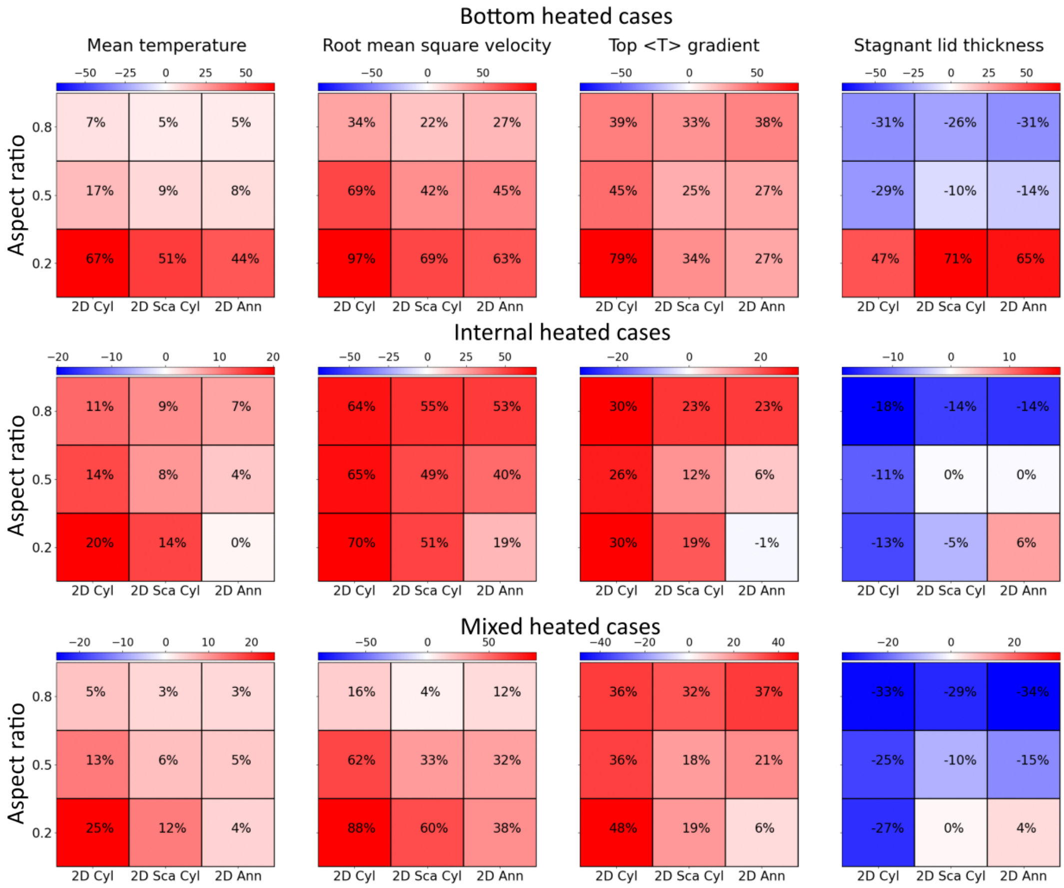

Figure 3: Averaged computed relative error to the 3D geometry with 3 different heating modes (i.e., purely basal heated, purely internal heated, and mixed heated) for steady-state convection simulations with a temperature dependent viscosity. The mean temperature of the domain, the root mean square velocity, the temperature gradient at the top of the domain, and the stagnant lid thickness are compared here. For each subplot analyzing the relative error in a given heating mode, every column represents a different geometry, namely the 2D cylinder, the 2D scaled cylinder, and the 2D spherical annulus. The thermal Rayleigh number is 5×10^6, the internal Rayleigh number is 5×10^7, and the investigated radius ratios are 0.2, 0.5, and 0.8.

3 Thermal evolution models

In this part we compare the 2D and 3D geometries in a more complex set-up, by using thermal evolution models in a stagnant lid regime. Compared to the previously discussed steady-state calculations, these models illustrate which of the 2D geometries can best reproduce the 3D results when mantle and core cooling are considered.

3.1 Mathematical model

For the thermal evolution models we use the Extended Boussinesq Approximation (EBA) (Schubert et al., 2001) to account for adiabatic heating and cooling. The energy equation (Eq. 3) becomes:

$$\frac{DT}{Dt} - \nabla \cdot (k \nabla T) - Di\alpha(T + T_{surf})\mathbf{u}_r - \frac{Di}{Ra}\Phi - H = 0, \tag{7}$$

where $\mathbf{u}_r$ is the radial component of the velocity vector, T_{surf} is the surface temperature, α is the thermal expansivity, and Φ is the viscous dissipation given by $\Phi = \tau : \dot{\varepsilon}/2$, where τ is the deviatoric stress tensor and $\dot{\varepsilon}$ the strain rate tensor. The dissipation number Di is defined as follows:

$$Di = \frac{\alpha_{ref} g_{ref} D}{c_p}, \tag{8}$$

where c_p is the mantle heat capacity.

In the thermal evolution models, we consider a temperature and pressure dependent viscosity that follows the Arrehnius law of diffusion creep. The non-dimensional equation for viscosity reads (Roberts & Zhong, 2006):

$$\eta(T, z) = exp\left(\frac{E + zV}{T + T_{surf}} - \frac{E + z_{ref}V}{T_{ref} + T_{surf}}\right), \tag{9}$$

where E and V are the activation energy and the activation volume respectively (Karato & Wu, 1993; Hirth & Kohlstedt, 2003). T_{ref} and z_{ref} are the reference temperature and depth, respectively, at which the reference viscosity is attained. The non-dimensional T_{ref} and z_{ref} values correspond to a dimensional reference temperature of 1600 K and a dimensional reference pressure of 3 GPa, respectively.

The temperature of the lower boundary T_{CMB} evolves following a 1-D energy balance, assuming a core with constant density and heat capacity (Stevenson et al., 1983):

$$c_c \rho_c V_c \frac{dT_{CMB}}{dt} = -q_c A_c, \tag{10}$$

where c_c is the heat capacity of the core, ρ_c is the core density, V_c is the core volume, q_c is the heat flux at the core-mantle boundary (CMB), and A_c is the core surface area. Here we do not consider core crystallization.

As appropriate for thermal evolution models, we take into account the decay of the heat producing elements (i.e., Ur^{238}, Ur^{235}, Th^{232}, and K^{40}). The amount of radioactive heat sources is calculated using the concentrations listed in Table 1.

In thermal evolution models we consider the effect of a 50 km laterally homogeneous crust. This crust is enriched in radiogenic elements while the mantle is depleted according to the following mass balance:

$$M_{tot} \cdot Q_{tot} = M_{mantle} \cdot Q_{mantle} + M_{crust} \cdot Q_{crust}, \tag{11}$$

where M is the mass and Q is the heating rate. This setup also considers the blanketing effect of the crust by using a lower thermal conductivity k in the crust compared to the mantle.

3.2 Case definition

We test three scenarios for the thermal evolution of a Mars-like, the Moon-like, and Mercury-like planet. We model the entire evolution of these planets to determine the variations over time of several key output quantities. These three planetary bodies were chosen because of their different interior structures. In the Mars-like case, the radius ratio between core and planetary radius is $f = 0.544$. The Moon- and Mercury-like scenarios represent two end-members in terms of their radius ratios, with $f = 0.224$ and $f = 0.828$, respectively.

In the case of the 2D grids, we use a radial resolution of ~ 10 km for Mars- and Moon-like cases, and a ~ 5 km radial resolution for the thin mantle of Mercury. In the case of the 3D grids, the radial resolution lies between 22 and 9 km, and we use a lateral resolution of 40962 points per shell. A more detailed list of the resolution for every grid is available in Table S2 of the SI.

In the cylindrical geometry, we use both the classical cylinder and the rescaling of van Keken (2001) as done previously in the stagnant lid steady-state simulations. It is worth to note that for the peculiar Moon-like interior structure, the scaling of the respective radii leads to a radius ratio $f = 0.0503$. Since this is an extreme case, we test whether the rescaling of the cylinder geometry is appropriate for such interior structures in a thermal evolution scenario.

It is important to note here that for each planet we use different Rayleigh numbers (i.e., Ra and Ra_Q). These are calculated self-consistently using the mantle thickness, internal heat sources, and temperature difference accross the mantle specific for each planet. The parameters are listed in Table 1. While for Mars- and Moon-like simulations we use a reference viscosity of 10^{21} Pa s, for the Mercury-like case we perform additional tests with a reference viscosity that is lower by two orders of magnitude (i.e., 10^{19} Pa s). Since the thin Mercurian mantle typically leads to a conductive state after a few Gyr of evolution, by using a lower reference viscosity we test additional scenarios, in which convection can be sustained over most of the evolution. The results for Mercury with $\eta_{ref} = 10^{21}$ Pa s and 10^{19} Pa s are also compared between the 3D spherical shell and the 2D geometries.

In all our simulations we consider the presence of a primordial crust with a thickness of 50 km, which is enriched in radiogenic elements compared to the bulk heat sources of the planet by a factor of 2 and has a two times lower thermal conductivity than the mantle (see Table 1). While being a representative value for the enrichment of the Mercurian crust (Tosi, Grott, et al., 2013), for the two other scenario it allows to increase the complexity of the simulation without having a thermal evolution dominated by the enrichment of the crust. A second set of thermal evolution models neglecting the effects of the crust is listed in Section S7 of the SI.

3.3 Results

In the following, we present the results obtained for the thermal history of Mars, the Moon, and Mercury for all geometries. Similar to the steady-state calculations, we show in Figure 3 the difference of the 2D cylinder, 2D scaled cylinder, and 2D spherical annulus to the 3D results after 4.5 Gyr of evolution (i.e., at present day). In addition to the error shown in percent, we also list the difference between the dimensional values for mean temperature, CMB temperature, root mean square velocity, lid thickness, as well as surface and CMB heat fluxes (Figure 4).

Figure 5 shows the entire evolution over 4.5 Gyr of the output quantities of interest for all four geometries (2D cylinder, 2D scaled cylinder, 2D spherical annulus, and 3D spherical shell) for a Mars-like geometry. Our results show clearly that in the case of a Mars-like geometry, the values obtained during the entire thermal evolution with

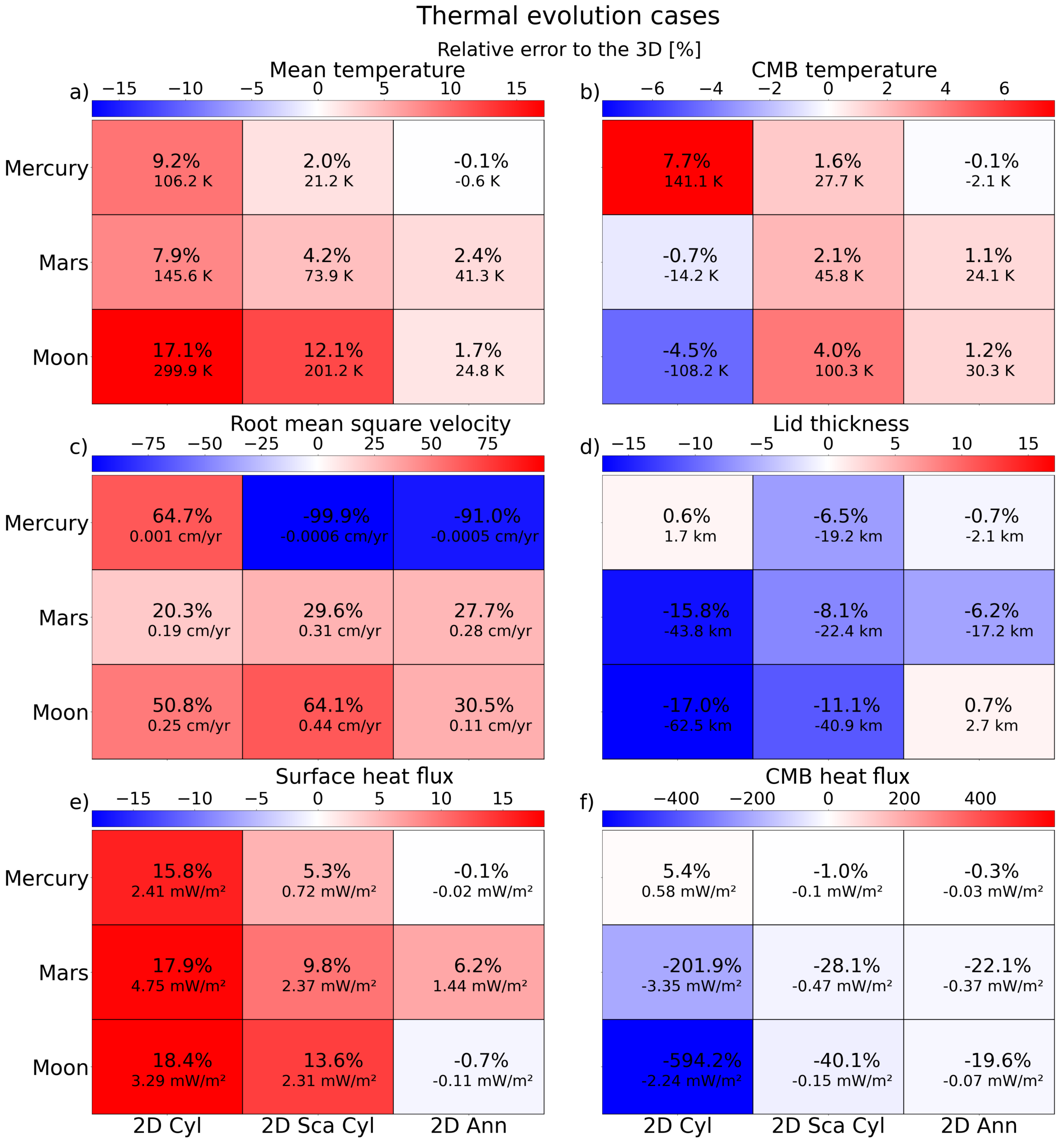

Figure 4: Relative error to the 3D in the case of thermal evolution simulations. In each panel we vary the planet on the y axis and on the x axis we vary the geometry. We investigate the relative error for: the mean temperature (a), the CMB temperature (b), the root mean square velocity (c), the stagnant lid thickness (d), the surface heat flux (e), and the CMB heat flux (f). A color in the blue indicates an underestimation of the results obtained in the 3D geometry whereas a color in the red indicates an overestimation. 2D Cyl stands for non-scaled 2D cylindrical geometry, 2D Sca Cyl is 2D cylindrical geometry with the scaling by van Keken (2001), and 2D Ann stands for 2D spherical annulus geometry. Each panel shows the relative error in % to the 3D and the absolute error in dimensional unit.

Symbol	Description (Unit)	Mars	Moon	Mercury
R_p	Planetary radius (km)	3400	1740	2440
R_c	Core radius (km)	1850	390	2020
D	Mantle thickness (km)	1550	1350	420
f	Radius ratio (-)	0.544	0.224	0.827
T_{surf}	Surface temperature (K)	220	250	440
T_{CMB}	CMB temperature (K)	2000	2000	2000
T_{ref}	Reference temperature (K)	1600	1600	1600
ΔT	Temperature contrast across the mantle (K)	1780	1750	1560
g	Gravitational acceleration ($m.s^{-2}$)	3.7	1.6	3.7
η_{ref}	Reference viscosity (Pas)	10^{21}	10^{21}	10^{21}
κ	Thermal diffusivity (m^2/s)	1×10^{-6}	1.06×10^{-6}	1.04×10^{-6}
α	Thermal expansivity (K^-1)	2.50×10^{-5}	2.50×10^{-5}	2.50×10^{-5}
Ra	Rayleigh number(-)	2.14×10^6	5.35×10^5	3.49×10^4
RaQ	Internal heating Rayleigh number (-)	5.91×10^7	8.70×10^6	8.00×10^4
ρ_{core}	Core density (kg/m^3)	6000	7500	6980
ρ_{mantle}	Mantle density (kg/m^3)	3500	3300	3380
ρ_{crust}	Crust density (kg/m^3)	2900	2700	2900
$c_{p,m}$	Mantle heat capacity (kgK)	1142	1142	1142
$c_{p,c}$	Core heat capacity (kgK)	850	850	850
V	Activation volume (m^3/mol)	6.00×10^{-6}	6.00×10^{-6}	6.00×10^{-6}
E	Activation energy (J/mol)	3.00×10^5	3.00×10^5	3.00×10^5
k_m	Mantle thermal conductivity ($Wm^{-1}K^{-1}$)	4	4	4
k_{cr}	Crust thermal conductivity ($Wm^{-1}K^{-1}$)	3	2	3
D_{crust}	Primordial crust thickness (km)	50	50	50
	Heat source concentration	(Taylor, 2013)	(Taylor, 1982)	(Padovan et al., 2017)
C_U	Uranium concentration (ppb)	16	33	7
C_{Th}	Thorium concentration (ppb)	58	125	29
C_K	Potassium concentration (ppm)	309	83	550

Table 1: Parameters for thermal evolution calculations for Mars, Moon, and Mercury. Note that the non-dimensional radii are rescaled according to Eq. 6 for the scaled cylinder geometry.

a 3D geometry are more closely reproduced by the spherical annulus than the cylinder, irrespective of whether it is scaled or not. It is to note that the spherical annulus geometry is reproducing especially well the evolution of the mean and core-mantle boundary temperatures (see Figure 4 for the actual present-day error), while the velocities are systematically overestimated by the 2D geometries (27.7% for the spherical annulus and 29.6% for the rescaled cylinder). This directly affects the calculation of the stagnant lid thickness, and thus underestimates it by 6.2% for the annulus and 8.1% for the rescaled cylinder. When trying to reproduce the heat fluxes at present day, the spherical annulus is somewhat better than the scaled cylinder, with an approximated underestimation of the CMB heat flux by 22% compared to 28% for the scaled cylinder, while the surface heat flux will be overestimated by 6% and 8% for the annulus and the scaled cylinder, respectively. While we focus in this part mostly on present-day values, when examining the entire thermal evolution of the planet we observe in the early and middle stages (between 1 and 3 Gyr) a relative error even larger as the one observed at present day, as seen on Figure 5c and e. The Mars-like setup is the most challenging setup to reproduce for the spherical annulus, and although exhibiting relatively low errors, it still shows the highest discrepancies between the thermal evolution cases with different interior structures. The overestimation of the mean temperature, mean velocity, surface heat flow, and underestimation of the stagnant lid thickness can be linked directly to the mixed heated, temperature-dependent viscosity simulation with a radius ratio of 0.5, which shows the same type of relative error (see Figure 3)

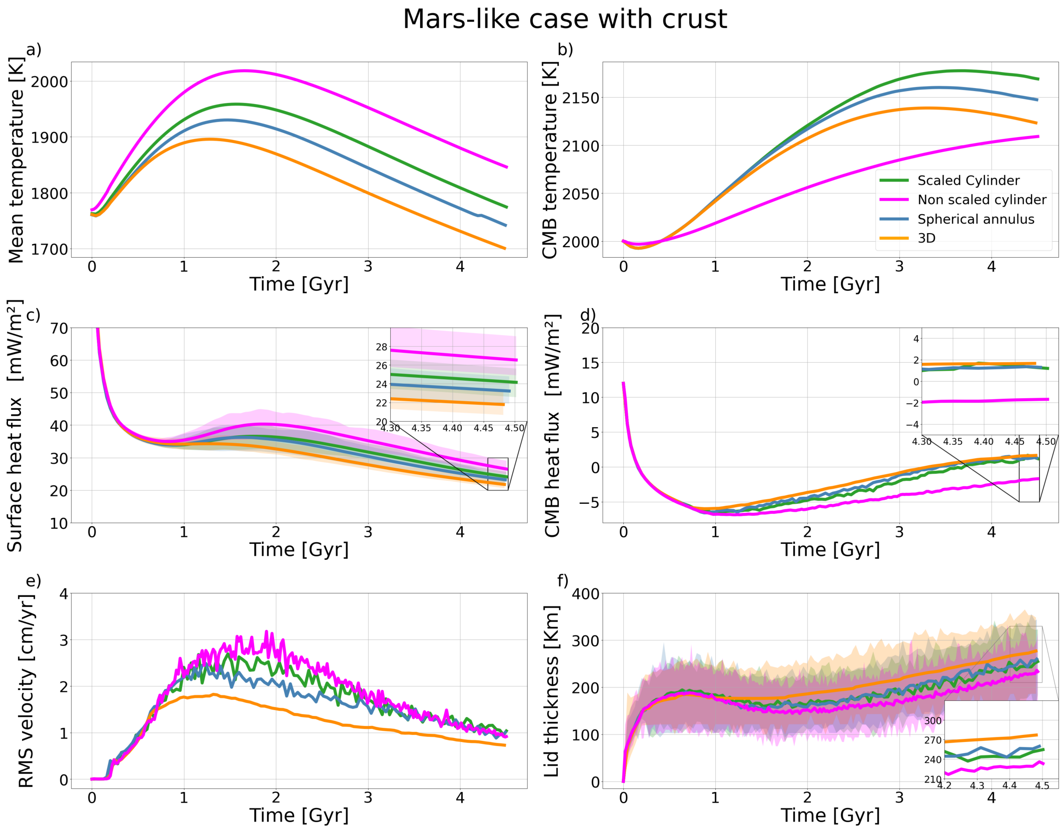

Figure 5: Timeseries of a Mars-like case with an initial crust of 50 km and with 4 different geometries (2D non-scaled cylindrical, 2D cylindrical, 2D spherical annulus and 3D spherical shell). The values shown here are the mean temperature (a), the core-mantle boundary temperature (b), the surface heat flux (c), the core-mantle boundary heat flux (d), the averaged root mean square velocity of the domain (e), and the lid thickness (f) from 4.5 Gyr ago to present day, respectively. The shaded areas show the min.-max. variations during the evolution. The non-scaled cylinder has been added to show the effect of the rescaling introduced by van Keken (2001).

In the case of a Moon-like setup (Figure 6) the differences between the spherical annulus and the cylinder are typically larger than in the Mars-like case. However the difference between the spherical annulus and the 3D is significantly lower in the case of the mean temperature, the stagnant lid thickness and the surface heat flow; as can be seen on Figures 6a, c, and f. The temperatures through time are very well reproduced by the spherical annulus (less than 2% of error compared to more than 12% for the cylindrical geometries). Similarly, the surface heat flux and the stagnant-lid thickness show a good match between the spherical annulus and the 3D geometries (see Table S5 of the SI). Concerning the cylindrical geometries, the effects of the rescaling are plainly visible on the overall temperatures and heat fluxes evolution. As van Keken (2001) showed, the cylinder tends to overestimate the relative importance of the CMB radius compared to planetary radius and requires a rescaling of the radii. However, for the very low aspect-ratio of the lunar mantle, even when the rescaling is applied the results are still largely different compared to a 3D spherical shell geometry. A better approximation of the 3D results is obtained by the spherical annulus, where such rescaling is not needed. We see that the CMB heat flux stays at around -1.86 mW m^{-2} even at present day, meaning that the core is actively heated by the mantle, although in the other geometries the core is already cooling (see Figure 6b and d), a behavior which is also seen for Mars with the non-scaled cylindrical geometry. Similar to what has been seen previously for the low aspect-ratio cases with temperature-dependent viscosity combining basal heating and internal heating (see Figure 3), the scaled and non-scaled cylindrical geometries show large disagreements in all studied metrics. Nevertheless, even in the spherical annulus, the mean velocity and the CMB heat flux present the largest errors among the investigated quantities.

In Figure 7, we show the results of the thermal evolution for a Mercury-like setup. Here we used two sets of simulations in order to illustrate the case of a initially weakly convecting mantle with a reference viscosity set as $\eta_{ref} = 10^{21}$ Pa s resulting in a Rayleigh number of $Ra = 3.49 \times 10^4$; and the case of a mantle presenting a stronger initial convection with a reference viscosity lowered by two orders of magnitude, thus increasing the Rayleigh number to $Ra = 3.49 \times 10^6$. Here again the global trend previously seen for Mars and the Moon emerges. As shown in figure 4, the spherical annulus geometry again reproduces best the 3D results with an approximate error of less than 1%, with a notable exception for the velocities, which are highly overestimated (more than 90% of relative error). The very high relative error of the v_{rms} is explained by the present-day state of the Mercurian mantle. In our simulations, a Mercury-like planet falls into a quasi-conductive state after a couple of Gyr of evolution irrespective of the geometry (Figure 7), which in turn gives very low absolute v_{rms} values. Yet the absolute difference of velocity between the geometry is very small (less than 1×10^3 cm/year). Despite these high relative error values in the velocities, the stagnant lid thickness is, however, quite well reproduced by the 2D geometries, giving a maximum relative error of 19 km (or an underestimation of 6.5%).

4 Discussion

Our results show that the spherical annulus can reproduce the 3D spherical shell geometry better than the cylindrical geometry, consistent with previous studies by Hernlund and Tackley (2008). Our systematic study, using simulations of increasing complexity, shows for the first time in great detail the difference in using a 2D geometry instead of a more realistic 3D spherical shell domain when modeling thermal convection in planetary mantles.

When using the cylindrical geometry, whether scaled or not, the results show substantial differences to the 3D geometry results in steady-state and thermal evolution simulations. The necessity of choosing between a scaled and a non-scaled cylinder in modeling geodynamic processes inevitably results in a trade-off between an accurate repre-

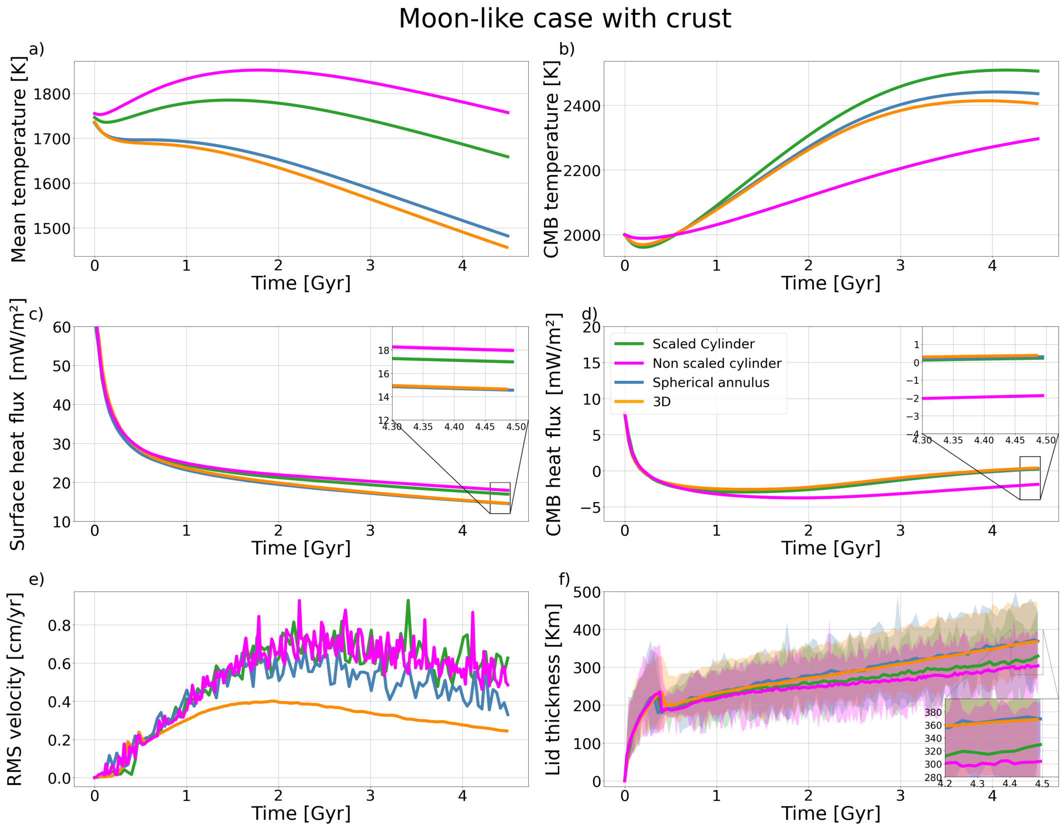

Figure 6: Timeseries of a Moon-like case with an initial crust of 50 km and with 4 different geometries (2D non-scaled cylindrical, 2D scaled cylindrical, 2D non-scaled cylindrical, 2D spherical annulus and 3D spherical shell). For a description off the values investigated, see Figure 5.

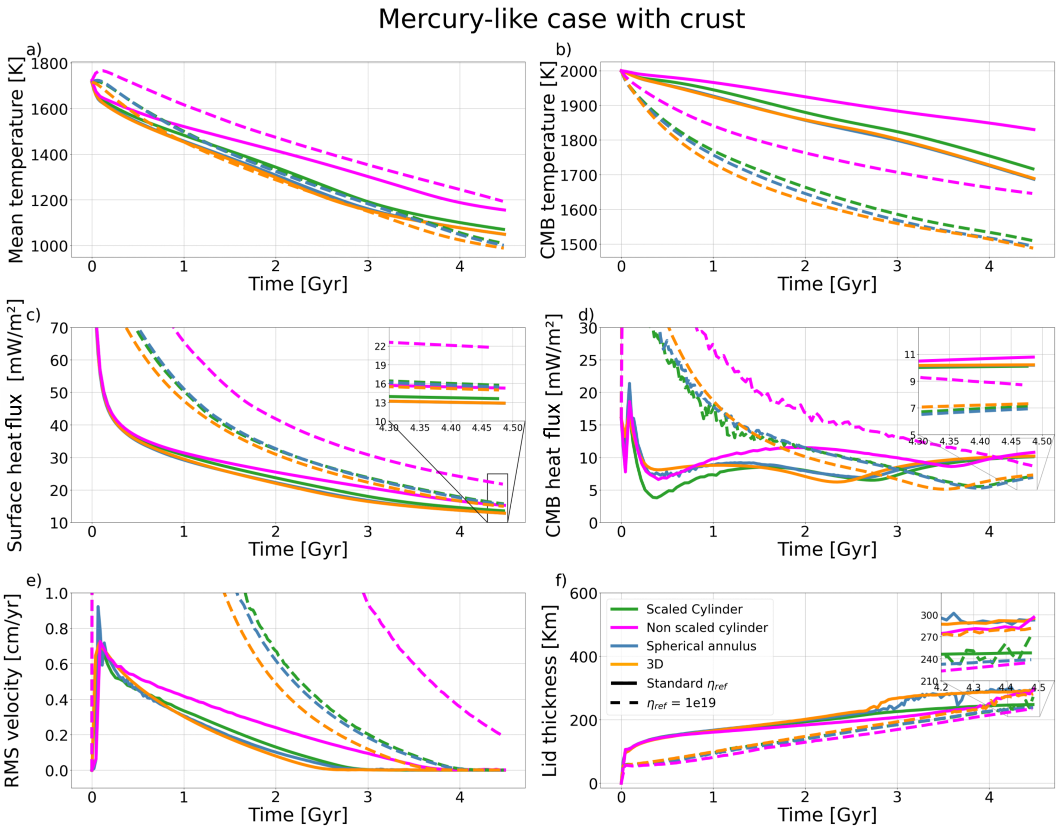

Figure 7: Timeseries of a Mercury-like case with an initial crust of 50 km, with 4 different geometries and 2 different reference viscosities. For a description off the values investigated, see Figure 5. The dotted lines represent simulations with a reference viscosity of η_{ref}=10^{19} Pa s while the solid lines represent the cases with a reference viscosity of η_{ref}=10^{21} Pa s. The maximum and minimum of the output quantities are not displayed here, since these variations are negligible.

sentation of the deep interior structures in the case of the non-scaled cylinder, especially important when studying thermochemical structures (Stegman et al., 2003; Nakagawa & Tackley, 2004; Yu et al., 2019; Kameyama, 2022), and a correct representation of the heat fluxes as well as root mean square velocity in the domain (Deschamps et al., 2010; Mulyukova et al., 2015) for the scaled one. To circumvent these inaccuracies, the systematic use of the spherical annulus in reproducing thermochemical convection in 3D is thus strongly recommended.

In the case of steady-state simulations, we showed that the spherical annulus has the largest error in the high radius ratio scenarios (i.e, $f = 0.6$ and 0.8). The efficiency of the spherical annulus in reducing the error to the 3D (compared to the results of the scaled cylinder) is most visible in the case of a low radius ratio configuration (i.e., $f = 0.2$), while nonetheless displaying large discrepancies in the mean temperature in the case of bottom heated and temperature-dependent setups, as also seen by Guerrero et al. (2018).

Concerning the heating modes, as reported by Hernlund and Tackley (2008), the purely internally heated cases show the largest difference between the 2D and 3D geometries, while the mixed heating cases (bottom and internal heating) tends to be the heating mode for which the spherical annulus exhibits the smallest errors in comparison to the spherical shell, as the difference in the temperature distribution between the spherical annulus and the spherical shell tends to disappear (see Figure S6 of the SI). This particularity becomes quite useful when trying to model more realistic processes such as thermal evolution models of terrestrial planets, as the silicate mantles of planets will invariably show heating induced by both the presence of radiogenic elements in the mantle and by the core. The smaller error between the 2D spherical annulus and 3D spherical shell observed in mixed heated cases makes the spherical annulus an acceptable alternative to model more complex scenario (Figure 4), for which a 3D geometry is too expensive. The trend of the relative error in the steady-state stagnant lid simulations with mixed heating is also observed in the case of thermal evolution models: the errors in the surface heat flux and stagnant lid thickness increase with increasing radius ratio (cf. the errors obtained for the Moon and Mars in Figure 4). However in the case of Mercury, while the steady-state simulations would predict the largest errors, the low Rayleigh number in thermal evolution models and the transition to a conductive state during the thermal evolution strongly reduce the discrepancy between 2D and 3D geometries.

The results presented here show that the spherical annulus is to be preferred to the cylindrical geometry, whether for steady-state simulations or thermal evolution simulations. However, in the case of the thermal evolution simulations one should question whether this geometry is sufficient to approximate the 3D spherical shell. Some observables such as the heat flux, the mechanical thickness of the lithosphere and the crust produced by partial melting of the mantle are used to evaluate the thermochemical evolution of a planet. But an important question is whether the 2D spherical annulus is accurate enough to reproduce the results of a 3D spherical shell for the above mentioned quantities, and which of these observables can be affected the most.

Additional post-processing has thus been conducted in order to better characterize the differences of more complex processes in the spherical annulus compared to the spherical shell. We exclude from this comparison the cylindrical geometry given its lack of accuracy in reproducing 3D. Moreover, the areas and volumes in the 2D cylindrical geometry are truly 2D and thus difficult to compare to the 3D spherical shell. Melting in the mantle, the thickness of the mechanical lithosphere, and heat fluxes are shown in Figure 8 as a function of time. For the calculation of the mechanical lithosphere thickness, we follow the approach of Grott and Breuer (2008). The calculations involving partial melting of the mantle are highly simplified and do not include the effects of latent heat or mantle depletion. While the quantities presented in Figure 8 are based on simple post-processing of the thermal evolution results, they are meant to provide first order implications for the thermal evolution modeling with 2D and 3D geometries (for additional information concerning the post processing, see S11, S12).

When reproducing 3D simulations, the spherical annulus is well suited to replicate melting, mechanical thickness and heat fluxes. In particular the heat fluxes, and especially the CMB heat flux (Figure 8g, h, i) are especially well reproduced in terms of values and trend of evolution. The largest errors were observed for a Mars-like structure with an overestimation of less than 1.5 $\mathrm{mW\,m^{-2}}$ compared to the 3D for the surface heat flux and an almost identical CMB heat flux (less than 1 $\mathrm{mW\,m^{-2}}$ lower values compared to the 3D case).

The mechanical thickness for a Moon-like interior structure will be underestimated on average by 5% for the spherical annulus, while the amount of melting will be overestimated by 10% as in the case of Mercury. Since the computation of the amount of partial melting in the mantle through time relies on the temperature profile of the simulation, it is not surprising to see on one hand the underestimation of the mechanical thickness and on the other hand a systematic overestimation of partial melting by the spherical annulus compared to the 3D. The main reason explaining these differences is that the spherical annulus will consistently overestimate the overall mantle temperature, leading to a hotter temperature profile, thus directly affecting the degree of melting and the thickness of the mechanical lithosphere.

In the case of a Mars-like structure (Figure 8b, e) the differences between 2D and 3D are larger, in particular in the case of partial melting, which the annulus will overestimate by a maximum of 30% at around 1.5 Gyr. The mechanical thickness will be underestimated on average by 10 %. In particular the differences in partial melting could lead to an overestimation of the crustal thickness in the 2D spherical annulus geometry. This in turn could lead to more crustal production due to a mechanism called "crustal blanketing" (e.g., Schumacher & Breuer, 2006), in which the reduced thermal conductivity of the crust will prevent efficient cooling of the mantle. A higher crustal production rate could then lead to a stronger depletion of the mantle in crustal components and volatile elements. Hence, care should be taken when the spherical annulus geometry is employed to study partial melting and subsequent crust production or degassing in particular for planets with an intermediate radius ratio, like Mars or Venus. These processes and the differences between 2D and 3D geometries for such scenarios need to be quantified in future studies.

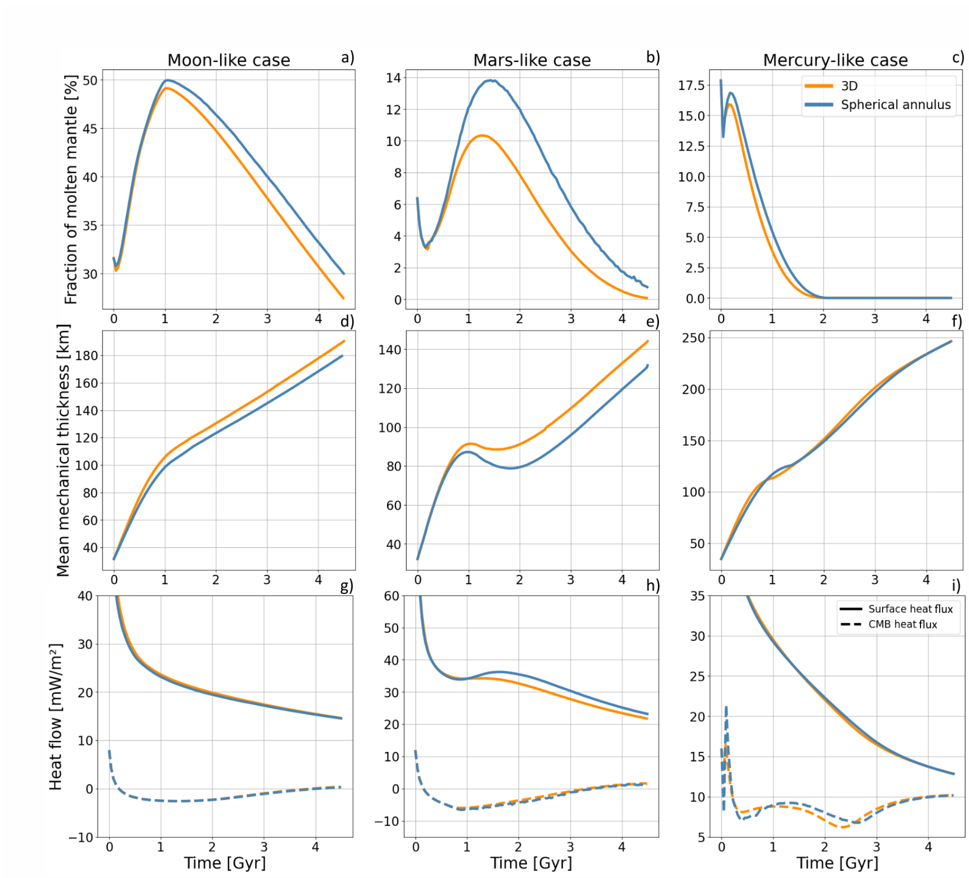

Figure 8: Timeseries of the three scenario investigated (from left to right; the Moon, Mars and Mercury). First row shows the fraction of molten mantle (in %) at a given time in the evolution for each planet, second row shows the mechanical thickness of the lithosphere (in km) during the evolution, and the third row shows the CMB and surface heat fluxes (in $\mathrm{mW\,m^{-2}}$). Since the cylindrical geometry shows the largest difference to the 3D, it was not included in this comparison. All the equations used in order to compute these quantities are described in the SI.

5 Conclusions

The main goal of this study is to provide a systematic comparison between different geometries in order to determine how accurate can 2D geometries reproduce 3D results. To this end, we investigated (scaled and non-scaled) 2D cylinder, 2D spherical annulus, and 3D spherical shell geometries in a series of scenarios. We started with isoviscous steady-state models, included the effects of a temperature dependent viscosity, and finally tested the different geometries for thermal evolution setups. Our main findings are the following:

1. While it is obvious that a 3D geometry should be preferred over a 2D one, due to the high computational cost, this may not always be feasible. Applying models with different complexities, we demonstrated that the 2D spherical annulus geometry is able to reproduce the 3D models much better than the 2D cylinder, in particular for the low radius ratio setups. The latter is also clearly seen when modeling the thermal evolution of the Moon.

2. For steady-state scenarios, our models show that the 2D geometries will mostly overestimate the mean temperature compared to 3D, a result largely explained by the geometry of mantle plumes (i.e., sheet-like in 2D vs. columnar-like in 3D). This discrepancy decreases with an increasing Rayleigh number but is more accentuated for low-radius ratio cases, a result already observed by Guerrero et al. (2018). The differences in temperature between the 2D and 3D geometries decreases for mixed heated cases (i.e., heated both from below and from within). This is especially true in the case of the spherical annulus, since the spherical annulus is a geometry which uses the same cell volumes as a 3D spherical shell.
3. We find that for intermediate ratios of the inner to outer radius (e.g., Mars-like thermal evolution case), the differences in the results for the 2D and 3D geometries are larger than for extreme radius ratios. In contrast to the temperature-dependent steady-state cases, where the difference in surface heat flux and stagnant lid thickness between 2D geometries and 3D geometries is largest for high radius ratios, the difference obtained for Mercury-like evolution parameters is minimal. This is due to the low Rayleigh number of Mercury that leads to the transition to a conductive state during its thermal history.
4. Care needs to be taken when studying melting processes with the spherical annulus in thermal evolution setups with intermediate radius ratios (e.g., Mars and Venus), as this geometry might overestimate crustal production by up to 30% compared to a 3D simulation leading to a different thermal history of the interior.

Future studies need to test the accuracy of the 2D spherical annulus in reproducing the 3D spherical shell geometry in more complex scenarios considering variable thermal conductivity and expansivity (Tosi, Yuen, et al., 2013), chemical buoyancy (Nakagawa et al., 2010), as well as partial melting of the mantle and its influence on thermal evolution.

Data Availability Statement

Supplementary datasets containing all values shown in tables and figures are available upon request on Zenodo : https://doi.org/10.5281/zenodo.8047757

Acknowledgments

Authors of this study gratefully acknowledge the financial support and endorsement from the DLR Management Board Young Research Group Leader Program and the Executive Board Member for Space Research and Technology. The authors also acknowledge the computational resources provided by the CARA cluster of the German Aerospace Center. Part of this work was performed on the HoreKa supercomputer funded by the Ministry of Science, Research and the Arts Baden-Württemberg and by the Federal Ministry of Education and Research.

References

Breuer, D., & Moore, W. B. (2015). Dynamics and Thermal History of the Terrestrial Planets, the Moon, and Io. *Treatise on Geophysics*, *10*(Second Ed.), 299–348. doi: 10.1016/B978-0-444-53802-4.00173-1

Deschamps, F., Tackley, P. J., & Nakagawa, T. (2010, July). Temperature and heat flux scalings for isoviscous thermal convection in spherical geometry. *Geophysical Journal International*, *182*(1), 137-154. doi: 10.1111/j.1365-246X.2010.04637.x

Frank-Kamenetskii, D. (1969). *Diffusion and Heat Transfer in Chemical Kinetics.*

Grott, M., & Breuer, D. (2008, 01). The evolution of the martian elastic lithosphere and implications for crustal and mantle rheology. *Icarus: International Journal of Solar System Studies*, *193*, 503-515.

Guerrero, J. M., Lowman, J. P., Deschamps, F., & Tackley, P. J. (2018). The influence of curvature on convection in a temperature-dependent viscosity fluid: Implications for the 2-d and 3-d modeling of moons. *Journal of Geophysical Research: Planets*, *123*(7), 1863-1880. Retrieved from `https://agupubs.onlinelibrary.wiley.com/doi/abs/10.1029/2017JE005497` doi: https://doi.org/10.1029/2017JE005497

Hernlund, J. W., & Tackley, P. J. (2008). Modeling mantle convection in the spherical annulus. *Physics of the Earth and Planetary Interios*, *171*, 48-54. doi: 10.1016/j.pepi.2008.07.037

Hirth, G., & Kohlstedt, D. (2003, January). Rheology of the upper mantle and the mantle wedge: A view from the experimentalists. *Washington DC American Geophysical Union Geophysical Monograph Series*, *138*, 83-105. doi: 10.1029/138GM06

Hüttig, C., & Stemmer, K. (2008a). Finite volume discretization for dynamic viscosities on Voronoi grids. *Physics of the Earth and Planetary Interios*, *171*(1–4), 137–146. doi: 10.1016/j.pepi.2008.07.007

Hüttig, C., & Stemmer, K. (2008b). The spiral grid: A new approach to discretize the sphere and its application to mantle convection. *Geochem. Geophys. Geosyst.*, *9*, Q02018. doi: 10.1029/2007GC001581

Hüttig, C., Tosi, N., & Moore, W. B. (2013). An improved formulation of the incompressible Navier-Stokes equations with variable viscosity. *Physics of the Earth and Planetary Interios*, *40*, 113–129.

Jarvis, G. T. (1993, March). Effects of curvature on two-dimensional models of mantle convection: Cylindrical polar coordinates. *JGR: Solid Earth*, *98*(B3), 4477-4485. doi: 10.1029/92JB02117

Jarvis, G. T., Glatzmaierand, G. A., & Vangelov, V. I. (1995, January). Effects of curvature, aspect ratio and plan form in two- and three-dimensional spherical models of thermal convection. *Geophysical and Astrophysical Fluid Dynamics*, *79*(1), 147-171. doi: 10.1080/03091929508228995

Kageyama, A., & Sato, T. (2004, 03). "yin-yang grid": An overset grid in spherical geometry. *Geochemistry Geophysics Geosystems*, *5*. doi: 10.1029/2004GC000734

Kameyama, M. (2022, 07). Numerical experiments on thermal convection of highly compressible fluids with variable viscosity and thermal conductivity in 2-D cylindrical geometry: implications for mantle convection of super-Earths. *Geophysical Journal International*, *231*(2), 1457-1469. Retrieved from https://doi.org/10.1093/gji/ggac259 doi: 10.1093/gji/ggac259

Karato, S. I., & Wu, P. (1993). Rheology of the upper mantle: a synthesis. *Science*, *260*, 771–778.

Mulyukova, E., Steinberger, B., Dabrowski, M., & Sobolev, S. V. (2015). Survival of llsvps for billions of years in a vigorously convecting mantle: Replenishment and destruction of chemical anomaly. *Journal of Geophysical Research: Solid Earth*, *120*(5), 3824-3847. Retrieved from https://agupubs.onlinelibrary.wiley.com/doi/abs/10.1002/2014JB011688 doi: https://doi.org/10.1002/2014JB011688

Nakagawa, T., & Tackley, P. J. (2004). Effects of a perovskite-post perovskite phase change near core-mantle boundary in compressible mantle convection. *Geophys. Res. Lett.*, *31*(L16611). doi: 10.1029/2004GL020648

Nakagawa, T., Tackley, P. J., Deschamps, F., & Connolly, J. A. D. (2010). The influence of MORB and harzburgite composition on thermo-chemical mantle convection in a 3-D spherical shell with self-consistently calculated mineral physics. *Earth Planet. Sci. Lett.*, *296*, 403–412. doi: 10.1016/j.epsl.2010.05.026

Noack, L., & Tosi, N. (2012). *High-performance modelling in geodynamics.* Integrated Information and Computing Systems for Natural, Spatial and Social Sciences.

Padovan, S., Tosi, N., Plesa, A.-C., & Ruedas, T. (2017). Impact-induced changes in source depth and volume of magmatism on Mercury and their observational signatures. *Nature communications*, *8*(1), 1945. doi: 10.1038/s41467-017-01692-0

Roberts, J. H., & Zhong, S. (2006). Degree-1 convection in the Martian mantle and the origin of the hemispheric dichotomy. *J. Geophys. Res. (Planets)*, *111*.

Schubert, G., Turcotte, D. L., & Olson, P. (2001). *Mantle convection in the Earth and planets.* Cambridge: Cambridge University Press.

Schumacher, S., & Breuer, D. (2006). Influence of a variable thermal conductivity on the thermochemical evolution of Mars. *J. Geophys. Res.*, *111*(E02006). doi: 10.1029/2007GL030083

Stegman, D. R., Jellinek, A. M., Zatman, S. A., Baumgardner, J. R., & Richards, M. A. (2003). An early lunar core dynamo driven by thermochemical mantle convection. *Nature*, *421*, 143–146.

Stevenson, D. J., Spohn, T., & Schubert, G. (1983). Magnetism and Thermal Evolution of the Terrestrial Planets. *Icarus*, *54*, 466–489.

Taylor, G. J. (2013). The bulk composition of mars. *Geochemistry*, *73*(4), 401–420.

Taylor, S. R. (1982, September). Lunar and terrestrial crusts: a constrast in origin and evolution. *Physics of the Earth and Planetary Interiors*, *29*(3-4), 233-241. doi: 10.1016/0031-9201(82)90014-0

Tosi, N., Grott, M., Plesa, A.-C., & Breuer, D. (2013). Thermo-chemical evolution of Mercury's interior. *J. Geophys. Res. (Planets)*. (accepted) doi: 10.1002/jgre.20168

Tosi, N., Yuen, D. A., de Koker, N., & Wentzcovitch, R. M. (2013). Mantle dynamics with pressure- and temperature-dependent thermal expansivity and conductivity. *Physics of the Earth and Planetary Interios*, *217*, 48–58. doi:

10.1016/j.pepi.2013.02.004
van Keken, P. E. (2001). Cylindrical scaling for dynamical cooling models of the earth. *Physics of the Earth and Planetary Interios*, *124*, 119–130.
van Keken, P. E., & Yuen, D. A. (1995). Dynamical influences of high viscosity in the lower mantle induced by the steep melting curve of perovskite: Effects of curvature and time dependence. *Journal of Geophysical Research: Solid Earth*, *100*(B8), 15233-15248. Retrieved from `https://agupubs.onlinelibrary.wiley.com/doi/abs/10.1029/95JB00923` doi: https://doi.org/10.1029/95JB00923
van Zelst, I., Crameri, F., Pusok, A. E., Glerum, A., Dannberg, J., & Thieulot, C. (2022). 101 geodynamic modelling: how to design, interpret, and communicate numerical studies of the solid Earth. *Solid Earth*, *13*(3), 583–637. Retrieved from `https://se.copernicus.org/articles/13/583/2022/` doi: 10.5194/se-13-583-2022
Yu, S., Tosi, N., Schwinger, S., Maurice, M., Breuer, D., & Xiao, L. (2019). Overturn of ilmenite-bearing cumulates in a rheologically weak lunar mantle. *Journal of Geophysical Research: Planets*, *124*(2), 418-436. Retrieved from `https://agupubs.onlinelibrary.wiley.com/doi/abs/10.1029/2018JE005739` doi: https://doi.org/10.1029/2018JE005739

Geochemistry, Geophysics, Geosystems

Supporting Information for

Supporting Information for "Approximating 3D Models of Planetary Evolution in 2D: A Comparison of Different Geometries"

Aymeric Fleury[1], Ana-Catalina Plesa[1], Christian Hüttig[1], Doris Breuer[1]

[1]Institute of Planetary Research, German Aerospace Center (DLR), Berlin, Germany

Contents of this file

Additional Supporting Information (Files uploaded separately)

1. Datasets concerning isoviscous simulations; Figure S5
2. Datasets concerning temperature dependent simulations; Figure S6
3. Datasets concerning thermal evolution simulations; Figure S7

Introduction

In Section S1 we present the scaling factors used in this study, as listed in Table S1. Section S2 displays in Table S2 all the parameters used to create the grids employed in this study for the thermal convection model GAIA. Section S3 details the differences between the cylindrical and the spherical annulus geometries used in our thermal convection code GAIA. Section S4 provides a short comparison between the study from *Hernlund and Tackley* (2008) and this study for isoviscous stead-state cases. Section S5 presents how the relative error is calculated. In Section S6 we give briefly the equations used for internal heating and the decay of heat producing elements in our model. In Sections S7 and S8 we list the tables displaying all the present-day values of the investigated output quantities for the thermal evolution scenario in an homogeneous setup (S7) and in a setup with a 50 km crust (S8); these data are available as CSV files provided at . Section S9 presents the temperature profiles at present day and at 1 Gyr into the evolution for each thermal evolution scenario with a 50 km crust. Section S10 shows the calculation of the stagnant lid thickness for the thermal evolution models. Section S11 displays the calculation of the partial melting in the mantle, as a post processing step for the thermal evolution models. Section S12 gives the formulation to calculate the thickness of the mechanical lithosphere as a post processing step. In the Section S13, three different comparisons of stagnant lid simulations (see Section 4), are displayed as slices for both the 3D spherical shell and the 2D spherical annulus geometry, with the 3D on the left and the 2D geometry on the right.

S1 Scaling table

The conservation equations used to model mantle convection are expressed in non-dimensional form. The non-dimensionalisation is obtained by multiplying the parameters by a well-suited scaling factor. Parameters with a star represent the non-dimensional ones and are calculated as follows:

Quantity	Non dimensional
Temperature	$T^* = \frac{T - T_0}{\Delta T}$
Length	$x^* = \frac{x}{D}$
Time	$t^* = \frac{\kappa_0}{D^2} t$
Velocity	$u^* = \frac{uD}{\kappa_0}$
Pressure	$P^* = \frac{PD^2}{\eta_0 \kappa_0}$
Stress	$\sigma^* = \sigma \frac{D^2}{\eta_0 \kappa_0}$
Density	$\rho^* = \frac{\rho}{\rho_0}$
Thermal expansivity	$\alpha^* = \frac{\alpha}{\alpha_0}$
Heat production rate	$H^* = \frac{HD^2}{\kappa_0 cp \Delta T}$
Viscosity	$\eta^* = \frac{\eta}{\eta_0}$
Activation energy	$E^* = \frac{E}{\Delta T R}$
Activation volume	$V^* = \frac{V \rho_0 D g}{\Delta T R}$

Table S1: Table of the non dimensional values used in the study

In the remainder of this study, all the non-dimensional parameters are used without the star for better readability.

Setup	Geometry	Aspect ratio	Radial resolution	Lateral resolution	Total points	Rayleigh number
Isoviscous	$2-D$	0.2	48 shells	227 p.per.shell	11350	$10^4 - 10^5 - 10^6$
	$2-D$	0.4	48 shells	352 p.per.shell	17600	$10^4 - 10^5 - 10^6$
	$2-D$	0.6	48 shells	604 p.per.shell	30200	$10^4 - 10^5 - 10^6$
	$2-D$	0.8	48 shells	1358 p.per.shell	67900	$10^4 - 10^5 - 10^6$
	$2-D$	0.2	120 shells	556 p.per.shell	69052	$10^7 - 10^8$
	$2-D$	0.4	120 shells	880 p.per.shell	107360	$10^7 - 10^8$
	$2-D$	0.6	120 shells	1508 p.per.shell	183976	$10^7 - 10^8$
	$2-D$	0.8	120 shells	3393 p.per.shell	413946	$10^7 - 10^8$
	$3-D$	0.2	48 shells	40962 p.per.shell	2048100	$10^4 - 10^5 - 10^6$
	$3-D$	0.4	48 shells	40962 p.per.shell	2048100	$10^4 - 10^5 - 10^6$
	$3-D$	0.6	48 shells	40962 p.per.shell	2048100	$10^4 - 10^5 - 10^6$
	$3-D$	0.8	48 shells	40962 p.per.shell	2048100	$10^4 - 10^5 - 10^6$
	$3-D$	0.2	70 shells	40962 p.per.shell	2949264	$10^7 - 10^8$
	$3-D$	0.4	70 shells	40962 p.per.shell	2949264	$10^7 - 10^8$
	$3-D$	0.6	70 shells	40962 p.per.shell	2949264	$10^7 - 10^8$
	$3-D$	0.8	70 shells	40962 p.per.shell	2949264	$10^7 - 10^8$
T-dependent	$2-D$	0.2	100 shells	472 p.per.shell	48144	$Ra = 5 \times 10^6; Ra_Q = 5 \times 10^7$
	$2-D$	0.5	100 shells	943 p.per.shell	96186	$-$
	$2-D$	0.8	100 shells	2828 p.per.shell	288456	$-$
	$3-D$	0.2	70 shells	40962 p.per.shell	2949264	$-$
	$3-D$	0.5	70 shells	40962 p.per.shell	2949264	$-$
	$3-D$	0.8	70 shells	40962 p.per.shell	2949264	$-$
Thermal evolution	$2-D$	Mars $\rightarrow$ 0.544117	155 shells	1 650 p.per.shell	259050	$Ra = 2.14 \times 10^6; Ra_Q = 5.91 \times 10^7$
	$3-D$	-	70 shells	40962 p.per.shell	2949264	$-$
	$2-D$	Moon $\rightarrow$ 0.224137	135 shells	670 p.per.shell	91790	$Ra = 5.35 \times 10^5; Ra_Q = 8.70 \times 10^6$
	$3-D$	-	64 shells	40962 p.per.shell	2703492	$-$
	$2-D$	Mercury $\rightarrow$ 0.827868	84 shells	2803 p.per.shell	241058	$Ra = 3.49 \times 10^4; Ra_Q = 8.00 \times 10^4$
	$3-D$	-	46 shells	40962 p.per.shell	1884252	$-$

Table S2: Grid parameters for each simulation in this study. For each grid, the number of shells displayed is the number of layers in the "active" part of the grid, meaning that it does not account for the two ghost layers at the base and at the top of the grid, which are used to set the boundary conditions.

S2 Grid parameters

This table provides all the grid parameters used in this study for the steady state simulations as well as the thermal evolution models.

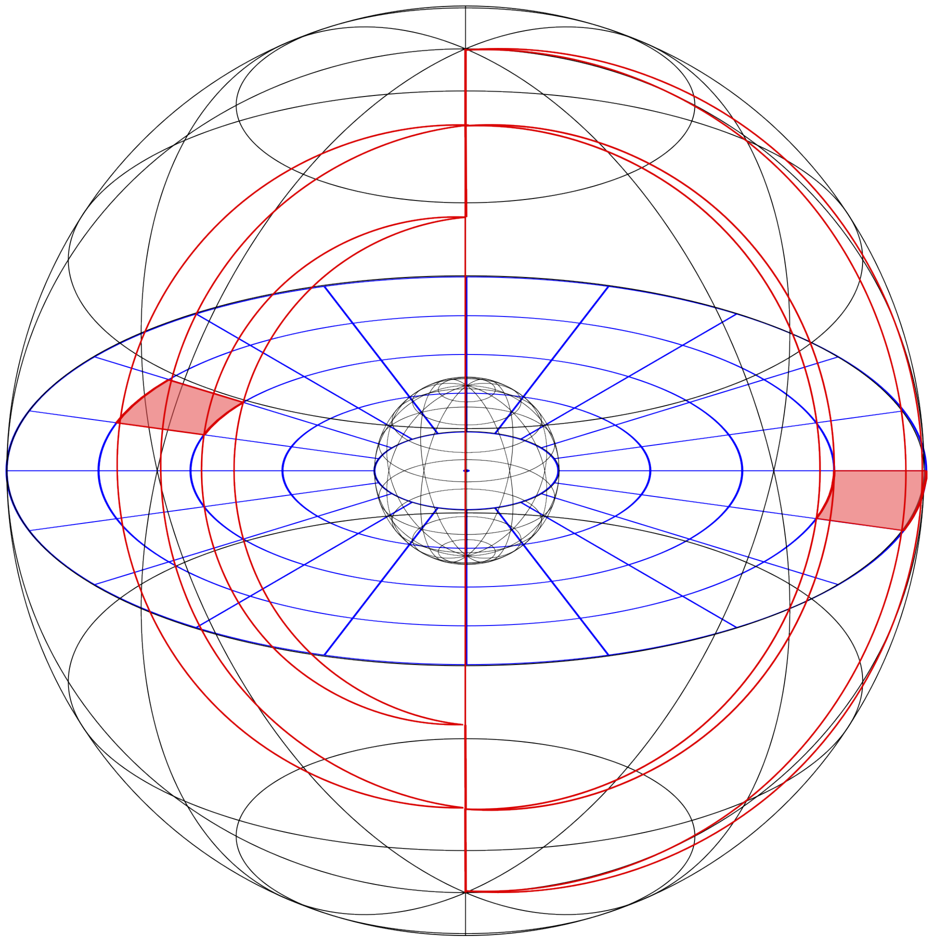

Figure S1: Representation of the elementary volumes of the cylinder in blue and of the spherical annulus in red. In a regular two dimensional representation of the spherical annulus grid, we only see the area of the elementary volume bisected by the equatorial plane (red filled areas).

S3 Spherical annulus geometry

The principal difference between the 2D spherical annulus and the 2D cylindrical geometry lies in the formulation of the areas and volumes for each grid. The cylindrical geometry will have a purely 2D formulation of its areas and volume whereas the spherical annulus use the same formulation as a 3D spherical shell. The effective degree of curvature for each cell goes then from 1 in the case of the cylinder to 2 in the case of the spherical annulus. For the mathematical formulation of the grid geometry, we refer to *Hernlund and Tackley*, 2008

S4 Comparison to results of Hernlund and Tackley 2008

This table presents the comparison between the study from *Hernlund and Tackley*, 2008 and this study for isoviscous steady state cases considering basal heating and internal heating, respectively, with Rayleigh numbers between $Ra = 10^4$ to $Ra = 10^5$. For the radius an Earth-like value is used (f= 0.55) for the 3D spherical shell and the annulus, while the scaled cylinder uses f= 0.3025. The values are averaged over the last 20% of the simulations.

		Bottom heated		
Ra = 10^4	Geometry	3D	Spherical annulus	Scaled cylindrical
Hernlund & Tackley 2008	v_{rms}	42.3	37.7	35.6
	v_{rms} peak-peak	0	0	0
	<Nu>	3.85	4.18	3.99
	<Nu> peak-peak	steady	steady	steady
This study	v_{rms}	42.1	43.1	37.3
	v_{rms} peak-peak	0	0	0
	<Nu>	3.84	4.12	4.08
	<Nu> peak-peak	steady	steady	steady
Ra = 10^5				
Hernlund & Tackley 2008	v_{rms}	160	160	165
	v_{rms} peak-peak	11	14	90
	<Nu>	7.27	7.39	6.2
	<Nu> peak-peak	0.5	0.3	2.1
This study	v_{rms}	163.9	160.0	158.1
	v_{rms} peak-peak	1	10	0
	<Nu>	6.62	7.16	7.75
	<Nu> peak-peak	0.03	0.4	0.2
		Internal heated		
Ra = 10^4	Ra_Q= 3.4×10^4			
Hernlund & Tackley 2008	v_{rms}	23.3	23.5	22.8
	v_{rms} peak-peak	0	0	0
	<T>	0.311	0.308	0.319
This study	v_{rms}	22.6	23.3	21.4
	v_{rms} peak-peak	0	0	0
	<T>	0.311	0.312	0.334
Ra = 10^5	Ra_Q= 6.6×10^5			
Hernlund & Tackley 2008	v_{rms}	60.5	78.5	77.0
	v_{rms} peak-peak	7	36	75
	<T>	0.322	0.349	0.384
This study	v_{rms}	76.7	84.6	79.7
	v_{rms} peak-peak	2.2	9	10.5
	<T>	0.337	0.3443	0.387

Table S3: Comparison of the spherical annulus used in this study and the study of *Hernlund and Tackley*, 2008. The top part of the table are the results from *Hernlund and Tackley*, 2008 and the bottom part of the table present the results from this study. The values displayed are the root mean square velocity (v_{rms}), mean temperature (<T>), and Nusselt numbers (Nu), which are computed once a statistical steady state is attained.

S5 Error computation

The error presented in the main manuscript to illustrate the difference between 2D and 3D geometries was computed as follows:

$$Error = -\frac{(3D_{value} - 2D_{value})}{max(3D_{value}; 2D_{value})} \times 100 \tag{S1}$$

The absolute error for the thermal evolution simulations on the other hand is calculated as:

$$Error = 2D_{dimensionalvalue} - 3D_{dimensionalvalue} \tag{S2}$$

in order to determine whether a 2D geometry over or under-estimates the 3D geometry results.

S6 Internal heating and heat producing elements decay

In our thermal evolution scenarii, we also take into account the decay of the heat producing elements, here being the Ur^{238}, Ur^{235}, Th^{232} and the K^{40}, thus giving us the heat production rate which is determined from present day amounts of heat sources and is given by equation 28 from *Breuer* (2009).

S7 Table of results for the thermal evolution simulations without crust

This table gives all the present-day values in a dimensional form for the thermal evolution simulations without crust.

Planet	Parameter (Unit)	3D sph. shell	2D sph. annulus	2D scaled cylinder	2D cylinder
Mars	T_{mean} (K)	1697.1	1713.9	1752.8	1846.3
	T_{CMB} (K)	2146.8	2150.2	2189.3	2171.1
	v_{rms} (cm/yr)	0.767	1.04	1.05	1.32
	q_{top} (mW/m^2)	21.68	22.95	24.10	27.12
	q_{bot} (mW/m^2)	2.10	2.12	1.91	1.07
	D_{lid} (km)	302.5	297.1	281.52	247.7
Moon	T_{mean} (K)	1367.6	1372.7	1552.6	1661.8
	T_{CMB} (K)	2379.7	2403.6	2473.2	2287.9
	v_{rms} (cm/yr)	0.216	0.374	0.527	0.472
	q_{top} (mW/m^2)	14.533	14.47	17.05	18.15
	q_{bot} (mW/m^2)	0.959	0.910	0.723	-3.35
	D_{lid} (km)	415.1	427.5	377.2	358.5
Mercury	T_{mean} (K)	1049.3	1048.0	1069.8	1155.6
	T_{CMB} (K)	1689.0	1685.1	1715.9	1829.2
	v_{rms} (cm/yr)	5.7E-4	3.1E-07	5.9E-07	7.7E-05
	q_{top} (mW/m^2)	12.85	12.83	13.56	15.29
	q_{bot} (mW/m^2)	10.20	10.15	10.10	10.74
	D_{lid} (km)	294.9	252.9	248.2	244.0

Table S4: Output quantities at present day for various geometries and planets in an homogeneous set.

S8 Table of results for the thermal evolution simulations with a 50 km crust
This table gives all the present-day values for the thermal evolution simulations with crust.

Planet	Parameter (Unit)	3-D sph. shell	2-D sph. annulus	2-D scaled cylinder	2-D cylinder
Mars	T_{mean} (K)	1700.4	1741.8	1774.4	1846.1
	T_{CMB} (K)	2123.4	2147.5	2169.2	2109.2
	v_{rms} (cm/yr)	0.73	1.00	1.03	0.92
	q_{top} (mW/m^2)	21.78	23.22	24.15	26.53
	q_{bot} (mW/m^2)	1.65	1.29	1.19	-1.68
	D_{lid} (km)	277.00	259.80	254.61	233.17
Moon	T_{mean} (K)	1456.9	1481.6	1658.1	1756.8
	T_{CMB} (K)	2404.7	2435.1	2504.9	2296.6
	v_{rms} (cm/yr)	0.24	0.35	0.68	0.50
	q_{top} (mW/m^2)	14.63	14.53	16.95	17.93
	q_{bot} (mW/m^2)	0.38	0.30	0.22	-1.86
	D_{lid} (km)	368.2	370.9	327.3	305.7
Mercury	T_{mean} (K)	1049.3	1048.7	1070.5	1155.5
	T_{CMB} (K)	1689.0	1686.9	1716.7	1830.1
	v_{rms} (cm/yr)	5.7E-04	5.1E-05	6.2E-07	1.6E-3
	q_{top} (mW/m^2)	12.8	12.8	13.6	15.2
	q_{bot} (mW/m^2)	10.2	10.1	10.8	10.1
	D_{lid} (km)	294.8	292.7	275.7	296.5

Table S5: Output quantities at present day for each planet in various geometries for the thermal evolution simulation with a 50km crust.

All the present day output quantities are available in the online CSV files of this study.

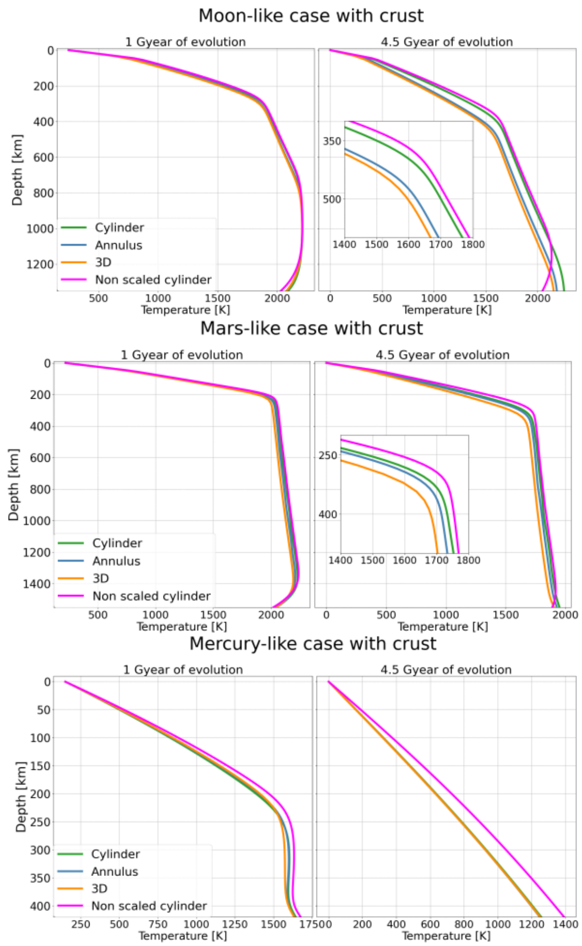

Figure S2: Profiles of temperature throughout the entire mantle for the Moon, Mars and Mercury. The profiles are shown at 1 billion years into the evolution and at present day. Every geometry studied is represented here; in the case of Mercury, only the simulations with a reference viscosity $\eta_{ref} = 10^{21}$ Pa s are shown.

S9 Temperature profiles for thermal evolution simulations

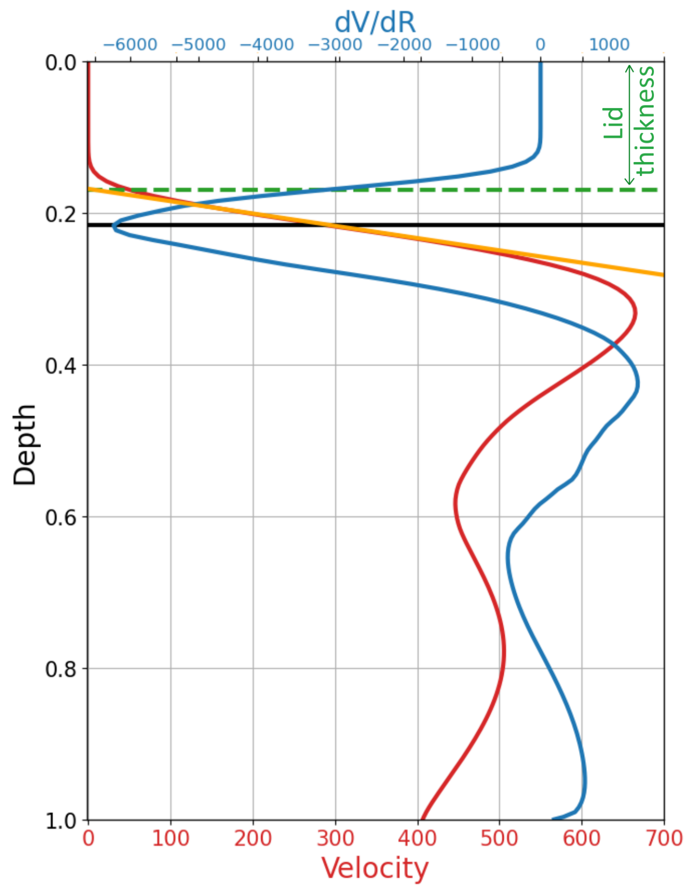

Figure S3: Calculation of the stagnant lid thickness adapted from the work of *Hüttig and Breuer* (2011). The thickness is determined by finding the depth where the derivative of the averaged velocity profile $\frac{dV}{dR}$ is the highest and intercepting it with the y axis. The red line is the averaged velocity profile in the domain, the blue line is the derivative of the velocity profile, the green dashed line is the depth of the stagnant lid, and the black line is the depth of the absolute value of the velocity derivative is the highest. All units are non dimensional.

S10 Stagnant lid calculation

In the calculation of the stagnant lid we use two different methods to determine its thickness. The first is from the work of *Hüttig and Breuer* (2011) and is illustrated by the Figure S3 The calculation of the stagnant lid becomes difficult with the velocity gradient method (*Hüttig and Breuer*, 2011) when the veolocity are too low. Therefore a second method, relying on the Peclet criterion is used in the case of Mercury when it falls into a quasi conductive state. The determination of the stagnant lid with a Peclet criterion, is determined with a threshold, that we set here as 5% of the averaged v_{rms} at the studied time step. The thickness is then the depth at which the v_{rms} profile becomes smaller than our threshold (or Peclet criterion).

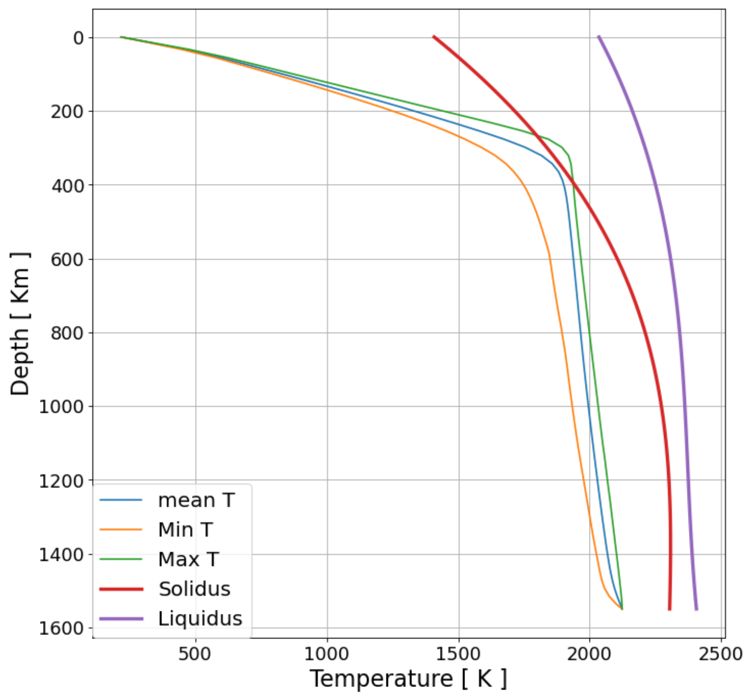

Figure S4: Melting curves from *Takahashi* (1990) and the minimum, mean and maximum temperature profile for a present-day Mars-like case.

S11 Partial melting calculation

We compute the averaged fraction of molten mantle at every time-step during the thermal evolution of the planet as a post processing step. It is used here as a simple comparison between the geometries. We use the melting curves from *Takahashi* (1990), as seen on Figure S2. However a cutoff is imposed at a depth of 7 GPa in the case of Mars. To calculate the volumetrically averaged degree of melting, we use eq 20. from *Morschhauser et al.* (2011) which is as following :

$$m_a = \frac{1}{V_a} \int_{V_a} \frac{T(r) - T_{sol}(r)}{T_{liq}(r) - T_{sol}(r)} \, dV, \tag{S3}$$

with V_a being the volume of the meltzone, T_{sol} the temperature of the solidus, T_{liq} the temperature of the liquidus, and $T(r)$ the calculated mantle temperature profile. We then compute the total volume of melted mantle and compare it with the total mantle volume.

Parameter	Crust	Mantle
$\dot{\epsilon}$ (s^{-1})	10^{-17}	10^{-17}
Q (kJ mol^{-1})	488	540
B (Pa^{-n} s^{-1})	1.1×10^{-26}	2.4×10^{-16}
n (-)	4.7	3.5
σ_y (MPa)	15	15

Table S6: Rheological parameters used in the equation S6, as appropriate for dry diabase crust and dry olivine mantle, for more information see *Plesa et al.* (2016), *Grott and Breuer* (2008).

S12 Mechanical thickness calculation

In this study we calculate the mechanical thickness, by using the strength envelope formalism *McNutt* (1984) for a structure comprised of a mantle layer and a crust layer. This mechanical thickness of the lithosphere represents the depth at which the plate looses its mechanical strength due to ductile flow *Grott et al.* (2007). This depth, or temperature equivalent is then calculated as following :

$$T_e = \frac{E}{R}\left[log\left(\frac{\sigma_B^n A}{\dot{\epsilon}}\right)\right]^{-1}, \tag{S4}$$

in which E, A and n are rheological parameter listed in Table S6, R is the gas constant, σ_B the bounding stress, and $\dot{\epsilon}$ being the strain rate. The total elastic thickness of this system depends then on whether the two layers act as a single elastic layer or are separated by an incompetent layer of crust. If the layers are separated, the elastic thickness D_e is then calculated as:

$$D_e = (D_{e,m}^3 + D_{e,c}^3)^{\frac{1}{3}}, \tag{S5}$$

where $D_{e,m}$ and $D_{e,c}$ are the thicknesses of the elastic parts of crust and mantle, respectively *Burov and Diament* (1995). However, if $D_{e,c}$ is greater or equals the local crustal thickness, then no layer of incompetent crust exists between the crust and the mantle and the effective elastic thickness is given by the sum of the two elastic layers:

$$D_e = D_{e,m} + D_{e,c} \tag{S6}$$

The decoupling of the system will strongly reduce the total elastic thickness as seen in eq. S5 and will mostly happen in regions with a thick crust. In the case of our simulations with a laterally homogeneous crust thickness we don't have any zone with a local thicker crust. To compute the local elastic thickness, a strain rate $\dot{\epsilon}$ profiles of 10^{-17} s^{-1} is used. The parameters used for this calculation are available in the Table S5.

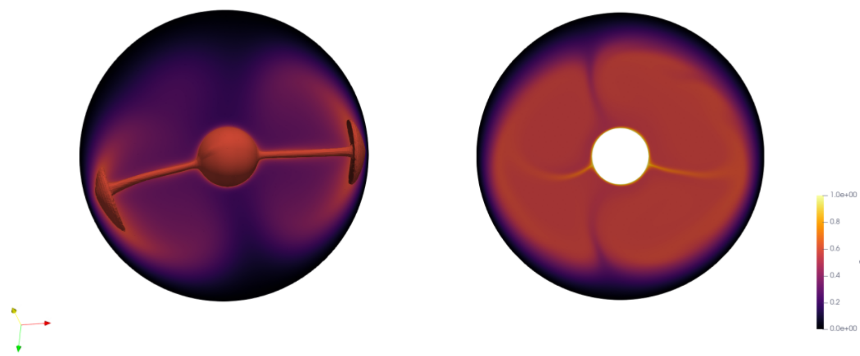

Figure S5: Temperature slices in a temperature-dependent viscosity case with purely basal heating, left is 3D spherical shell and right is 2D spherical annulus. Two plumes are present in both geometries, however the distribution of the temperature is much more diffuse in the case of the annulus, as seen in *Guerrero et al.* (2018).

S13 Slices comparison 3D-2D in stagnant lid simulations

The plots presented here show special cases of comparison between 3D and 2D spherical annulus for different heating mode in temperature-dependent viscosity setups.

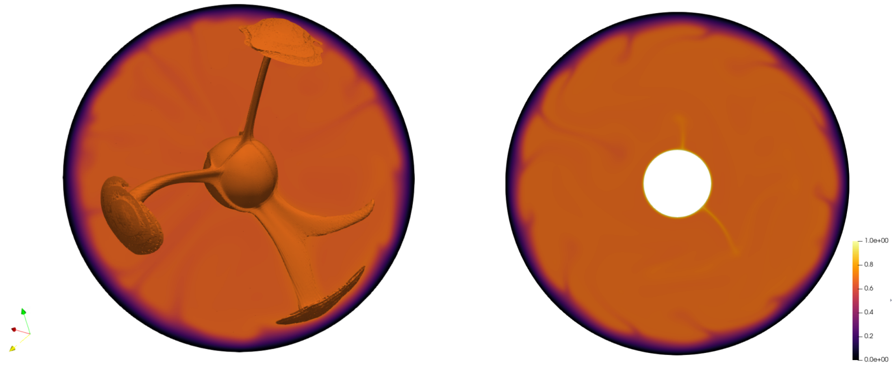

Figure S6: Temperature slices in a temperature-dependent viscosity case with basal and internal heating. We note the disappearance of the error of the temperature distribution seen in Figure S1 by the addition of internal heating.

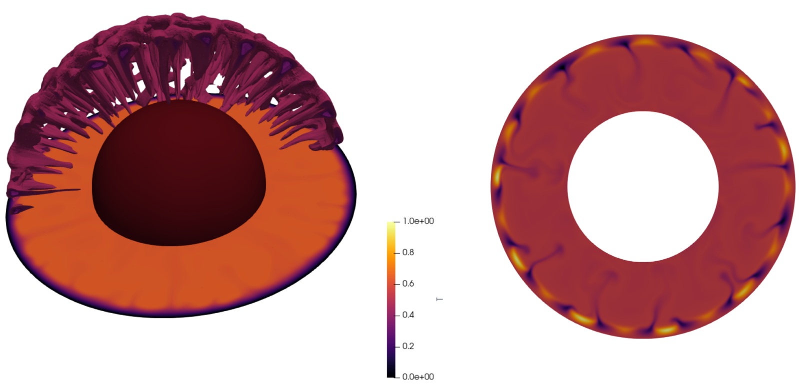

Figure S7: Temperature slices in a temperature-dependent viscosity case with purely internal heating. The amount of downwellings in a slice for the 3D case is far larger than what can be seen for the 2D spherical annulus (2D).

Supplementary datasets
The following datasets are available upon request on Zenodo :
https://doi.org/10.5281/zenodo.8047757

Datasets concerning isoviscous simulations
Tables containing the time averaged (on the last 10% of the run) values for all the outputs and geometry studied. There is one table per *Ra* number with a given heating mode. In total there are 15 tables for each scenarios (i.e., three different heating modes and five different *Ra* numbers).

Datasets concerning temperature dependent simulations
Tables containing the time averaged (on the last 10% of the run) values for all the outputs and geometry studied for temperature dependent viscosity simulations. Only one *Ra* is investigated. In total three tables, for three heating modes.

Datasets concerning thermal evolution simulations with and without crust
Tables containing dimensional present day values of all the investigated outputs for different geometries and planet scenarios for cases with and without crust. In total six tables, for three planets.

References

Breuer, D., 4.2.3.4 dynamics and thermal evolution: Datasheet from landolt-börnstein - group vi astronomy and astrophysics · volume 4b: "solar system" in springermaterials (https://doi.org/10.1007/978-3-540-88055-4_19), doi:10.1007/978-3-540-88055-4_19, copyright 2009 Springer-Verlag Berlin Heidelberg, 2009.

Burov, E.-B., and M. Diament, The effective elastic thickness (Te) of continental lithosphere: What does it really mean?, *J. Geophys. Res.*, *100*, 3905–3927, 1995.

Grott, M., and D. Breuer, The evolution of the Martian elastic lithosphere and implications for crustal and mantle rheology, *Icarus*, *193*, 503–515, doi:10.1016/j.icarus.2007.08.015, 2008.

Grott, M., J. Helbert, and R. Nadalini, Thermal structure of Martian soil and the measurability of the planetary heat flow, *J. Geophys. Res.*, *112*, E09,004, doi:10.1029/2007JE002905, 2007.

Guerrero, J. M., J. P. Lowman, F. Deschamps, and P. J. Tackley, The influence of curvature on convection in a temperature-dependent viscosity fluid: Implications for the 2-d and 3-d modeling of moons, *Journal of Geophysical Research: Planets*, *123*(7), 1863–1880, doi:https://doi.org/10.1029/2017JE005497, 2018.

Hernlund, J. W., and P. J. Tackley, Modeling mantle convection in the spherical annulus, *Physics of the Earth and Planetary Interios*, *171*, 48–54, doi:10.1016/j.pepi.2008.07.037, 2008.

Hüttig, C., and D. Breuer, Regime classification and planform scaling for internally heated mantle convection, *Physics of the Earth and Planetary Interios*, *186(3-4)*, 111–124, 2011.

McNutt, M. K., Lithospheric flexure and thermal anomalies, *J. Geophys. Res.: Solid Earth*, *89*(B13), 11,180–11,194, doi:10.1029/JB089iB13p11180, 1984.

Morschhauser, A., M. Grott, and D. Breuer, Crustal recycling, mantle dehydration, and the thermal evolution of Mars, *Icarus*, *212*, 541–558, doi:10.1016/j.icarus.2010.12.028, 2011.

Plesa, A.-C., M. Grott, N. Tosi, D. Breuer, T. Spohn, and M. A. Wieczorek, How large are present-day heat flux variations across the surface of Mars?, *J. Geophys. Res.*, *121*(12), 2386–2403, doi:10.1002/2016JE005126, 2016.

Takahashi, E., Speculations on the archean mantle: Missing link between komatiite and depleted garnet peridotite, *J. Geophys. Res.*, *95(B10)*, 15,941–15,954, 1990.